Geophysical Journal International

Geophys. J. Int. (2021) **226,** 1368–1389
Advance Access publication 2021 May 01
GJI Geomagnetism, Rock Magnetism and Palaeomagnetism

doi: 10.1093/gji/ggab177

Magnetic fabric from Quaternary volcanic edifices in the extensional Bransfield Basin: internal structure of Penguin and Bridgeman islands (South Shetlands archipelago, Antarctica)

B. Oliva-Urcia [1], J. López-Martínez,[1] A. Maestro,[1,2] A. Gil,[3] T. Schmid,[4] L.J. Lambán,[5] C. Galé,[3] T. Ubide [6] and M. Lago[3]

[1] *Department of Geology and Geochemistry, Faculty of Sciences, Universidad Autónoma de Madrid,* 28049 *Madrid, Spain. E-mail: belen.oliva@uam.es*
[2] *Instituto Geológico y Minero de España,* 28760 *Tres Cantos, 28003 Madrid, Spain*
[3] *Earth Sciences Department, Geotransfer-IUCA, Universidad de Zaragoza,* 50009 *Zaragoza, Spain*
[4] *Centro de Investigaciones Energéticas, Medioambientales y Tecnológicas (CIEMAT),* 28040 *Madrid, Spain*
[5] *Instituto Geológico y Minero de España, Oficina de Zaragoza,* 50006 *Zaragoza, Spain*
[6] *School of Earth and Environmental Sciences, The University of Queensland, St Lucia* 4072*, Queensland, Australia*

Accepted 2021 April 29. Received 2021 April 28; in original form 2020 December 4

SUMMARY

Studying the magnetic fabric in volcanic edifices, particularly lava flows from recent eruptions, allows us to understand the orientation distribution of the minerals related to the flow direction and properly characterize older and/or eroded flows. In this work, the magnetic fabric from recent (Quaternary) lava flows (slightly inclined in seven sites and plateau lavas in two sites), pyroclastic deposits (two sites from a scoria cone) and volcanic cones, domes and plugs (three sites) from Penguin and Bridgeman islands, located in the Bransfield backarc basin, are presented. The volcanism in the two islands is related to rifting occurring due to the opening of the Bransfield Strait, between the South Shetlands archipelago and the Antarctic Peninsula. The direction of flow of magmatic material is unknown. Rock magnetic analyses, low temperature measurements and electron microscope observations (back-scattered electron imaging and Energy Dispersive X-ray analyses) reveal a Ti-poor magnetite (and maghemite) as the main carrier of the magnetic fabric. Hematite may be present in some samples. Samples from the centre of the lavas reveal a magnetic lineation either parallel or imbricated with respect to the flow plane, whereas in the plateau lavas the magnetic lineation is contained within the subhorizontal plane except in vesicle-rich samples, where imbrication occurs. The magnetic lineation indicates a varied flow direction in Bridgeman Island with respect to the spreading Bransfield Basin axis. The flow direction in the plateau lavas on Penguin Island is deduced from the imbrication of the magnetic fabric in the more vesicular parts, suggesting a SE–NW flow. The volcanic domes are also imbricated with respect to an upward flow, and the bombs show scattered distribution.

Key words: Magnetic properties; Antarctica; Magnetic fabrics and anisotropy; Lava rheology and morphology.

1 INTRODUCTION

Magnetic fabric is a geophysical approach to unravel the orientation distribution of grains in rocks, sediments or soils (Tarling & Hrouda 1993; Borradaile & Jackson 2004, and references therein). It is a relatively fast technique after sampling a ∼10 cm^3 of oriented material. After measuring the anisotropy of the magnetic susceptibility (AMS, or magnetic fabric), a symmetric second rank tensor is defined, that can be represented by an ellipsoid. This is defined by three mutually perpendicular axes (maximum, intermediate and minimum) and different parameters involving the axes (magnitude and shape of the ellipsoid) and the orientation of the magnetic ellipsoid (Tarling & Hrouda 1993).

Particularly, in magmatic rocks, numerous studies have been carried out using magnetic fabric in order to (i) decipher the strain during the emplacement of magmatic bodies in the crust (e.g. Bouchez 1997; Román-Berdiel *et al.* 1998, 2004; Sant'Ovaia *et al.* 2001; Aranguren *et al.* 2003), (ii) to infer magma flow in dykes (e.g. Archanjo & Launeau 2004; Stevenson *et al.* 2008; Soriano *et al.* 2016; Nagaraju & Parashuramulu 2019) or (iii) to analyse the internal structure of lavas either to discover the flow direction (Plenier *et al.* 2005; Boiron *et al.* 2013), subsequent deformation/tilting

(Henry *et al.* 2003; Fanjat *et al.* 2012; Pueyo-Anchuela *et al.* 2014), or to infer the relationship between the magnetic and the crystallographic fabrics, taking into account the crystallization process within the flow (Bascou *et al.* 2005) or the viscosity of the flow (Hrouda *et al.* 2005).

The magnetic fabric in lavas can unravel heterogeneous deformation related to rheology, flow dynamics and lava flow-induced shear strain, which can lead to the development of different magnetic fabric types (zones) in the same lava flow (Cañón-Tapia 2004; Caballero-Miranda *et al.* 2016, and references therein). The expected model of the 'normal' magnetic fabric in a lava is that the magnetic lineation coincides with the flow direction whereas the minimum axis of the magnetic ellipsoid is perpendicular to the surface of the lava flow (Bascou *et al.* 2005 and references therein). Other orientations found in different zones of a thick lava flow explain the apparent contradictions found in earlier works (Cañón-Tapia 2004), since magnetic lineations (orientation of the long axes of the magnetic ellipsoid) were found mostly parallel to the flow direction, but also perpendicular or with other directions (Hrouda *et al.* 2005, and references therein). These 'abnormal' magnetic fabric have been related to for example, single domain ferromagnetic grains (inverse fabric), magnetic interactions, location near the lava boundaries (imbrication as in dykes), steep palaeoslopes or flow dynamics (Bascou *et al.* 2005; Fanjat *et al.* 2012, and references therein; Caballero-Miranda *et al.* 2016, and references therein).

The studies of magnetic fabric in recent lavas are useful to identify single flows in older or partially eroded lava flows (Caballero-Miranda *et al.* 2016), and to detect different rates of shear, depending on the position in a flow, therefore enabling inferences to the local flow direction and aspects related to the velocity field of each flow (Cañón-Tapia *et al*. 1997). Other studies suggest that a better constraint for a basaltic lava flow is by the magnetic plane (a plane which contains the maximum and intermediate magnetic axes, Boiron *et al.* 2013). In general, the flow of the lava relates to the magnetic foliation plane and the plunge of the magnetic lineation (k_{max} axes), with near vertical minimum magnetic axes (k_{min} axes) and the maximum magnetic axes (k_{max} axes) near horizontal positions parallel or perpendicular to the flow (Caballero-Miranda *et al.* 2016, and references therein). Therefore, magnetic fabric is useful when other flow markers are not present and little is known on the emplacement conditions or source location (Hrouda *et al.* 2005).

In this work, new magnetic fabric results from Quaternary magmatic material from Bridgeman and Penguin islands are presented. These islands are located in the Bransfield backarc basin, in the northern part of the Antarctic Peninsula, a particularly signified and active area of Late Cenozoic Antarctic volcanism. Volcanic studies in this area have focused mainly on Deception Island (e.g. Baraldo *et al*. 2003; Maestro *et al.* 2007; Pueyo-Anchuela et al 2014; Oliva-Urcia *et al.* 2015; Smellie *et al.* 2021), but knowledge about the magnetic properties of the volcanic rocks in the other islands is scarce (Pańczyk & Nawrocki 2011) or non-existent. In particular, the samples analysed and studied from Bridgeman and Penguin islands consist of seven lava flows on Bridgeman Island, and two pyroclastic (lapilli, bombs) rocks, three magmatic domes and plugs and two lava flows on Penguin Island. In combination with standard rock magnetic analyses (thermomagnetic curves, hysteresis loops and isothermal remanent magnetization curves), electronic microscope observations have been carried out in order to identify the main carrier of the magnetic fabric, its orientation distribution and the interpretation in relation to the geological setting and flow direction of magmatic material. The new AMS data aims to determine possible flow directions and to exemplify the usefulness of magnetic fabric for the study of incomplete or eroded older lava flows.

2 GEOLOGICAL SETTING AND SAMPLING LOCATION

The volcanism in the Bransfield back-arc basin (also known as Bransfield Strait or Bransfield Trough) is related to the rifting on the northern tip of the Antarctic Peninsula, due to the subduction and roll-back of the former Phoenix Plate towards the south, under the South Shetlands Block, combined with the eastward motion of the Scotia Plate along the South Scotia Ridge (Barker 1982; Maldonado *et al.* 1994; González-Casado *et al.* 2000; Galindo-Zaldívar *et al.* 2006; Maestro *et al.* 2007, and references therein, Figs 1 and 2). The Scotia Plate is enclosed by the Scotia Arc, a megastructure composed by seamounts, submarine ridges and islands connecting South America to the Antarctic Peninsula (Barker 2001; Bohoyo *et al.* 2019).

Rifting in the Bransfield Basin started in the late Cenozoic (González-Ferrán 1985) and is still active in the narrow and NE–SW elongated basin (500 km long, 100 km wide and 2000 m water depth, Fisk 1990; Catalán *et al.* 2013). The Bransfield Basin has seismic and volcanic activity, and geophysical data indicate a thinned crust, hydrothermal activity and a large negative magnetic anomaly (Gràcia *et al.* 1996, and references therein). The basin is subdivided into three parts (west, central and east). Recent models using magnetic and gravity data analyses reinforce that the central part of the basin 'is in a rifting in its latest stages or presents an incipient oceanic crust formed by recent oceanic spreading' (Catalán *et al.* 2013 as noted previously in Gràcia *et al.* 1996; Keller *et al.* 2002).

There are two subaerial volcanoes near the rift axis in the Central Bransfield Basin (Bridgeman—in the East—and Deception—in the West—islands), together with submarine volcanic edifices forming a discontinuous neovolcanic ridge roughly aligned with the subaerial volcanic islands (Gràcia *et al.* 1996; Keller *et al.* 2002; Fretzdorff *et al.* 2004; Catalán *et al.* 2013). In addition, there are two subaerial volcanic edifices on the norther margin of the basin (Melville Peak and Penguin Island) in and near King George Island, respectively (Fig. 2).

The composition of the Quaternary volcanism in the Bransfield Basin ranges from basaltic andesite (similar to island arc tholeiite), tholeiite (similar to mid-ocean ridge basalt—MORB) to volcanic island with basalt-to-trachydacite suite (Keller *et al.* 2002, and references therein), that is, a wide compositional spectrum (Fretzdorff *et al.* 2004; Galé *et al.* 2014). The geochemical variations are not systematic along the axis of the basin, which suggests a non-unidirectional propagation of rifting (Keller *et al.* 2002). Major and trace elements allow distinguishing up to three geochemical groups from the Central and East Bransfield Basin, being the subalkaline group (from basalt to rhyolite), where the low-K series is the predominant composition (Fretzdorff *et al.* 2004; Kraus *et al.* 2013).

Petrology has been previously studied in the two selected Penguin and Bridgeman islands (Pańczyk & Nawrocki 2011; Kraus *et al.* 2013, and references therein). In addition, radiometric and palaeomagnetic analyses have been carried out on Penguin Island (Pańczyk & Nawrocki 2011). As seen in Fig. 2, Penguin Island is located north of the present rifting axis but also related to the opening of the Bransfield Basin. It is a small island (1.8 km^2) defined as a stratocone (Deacon Peak, a basaltic scoria cone with a height

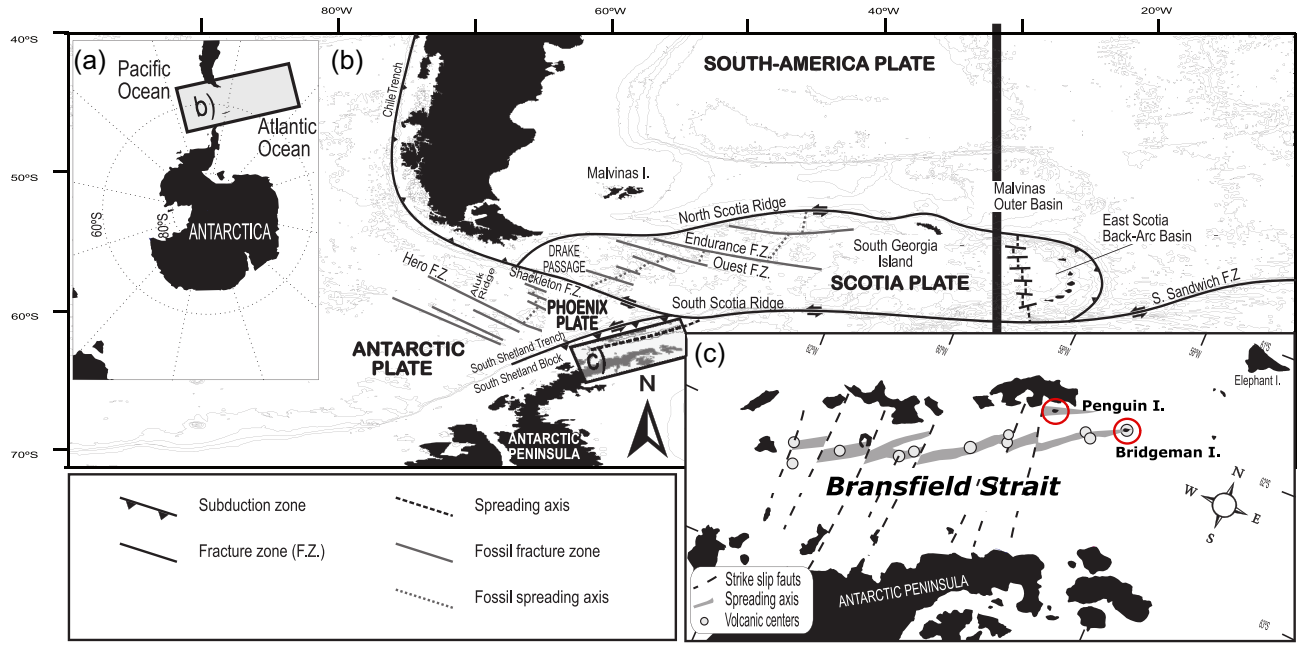

Figure 1. Location of. (a) General setting, (b) geotectonic setting and (c) location of the Bransfield Strait and the two studied islands (see also Fig. 2). Modified from Maestro *et al.* (2007).

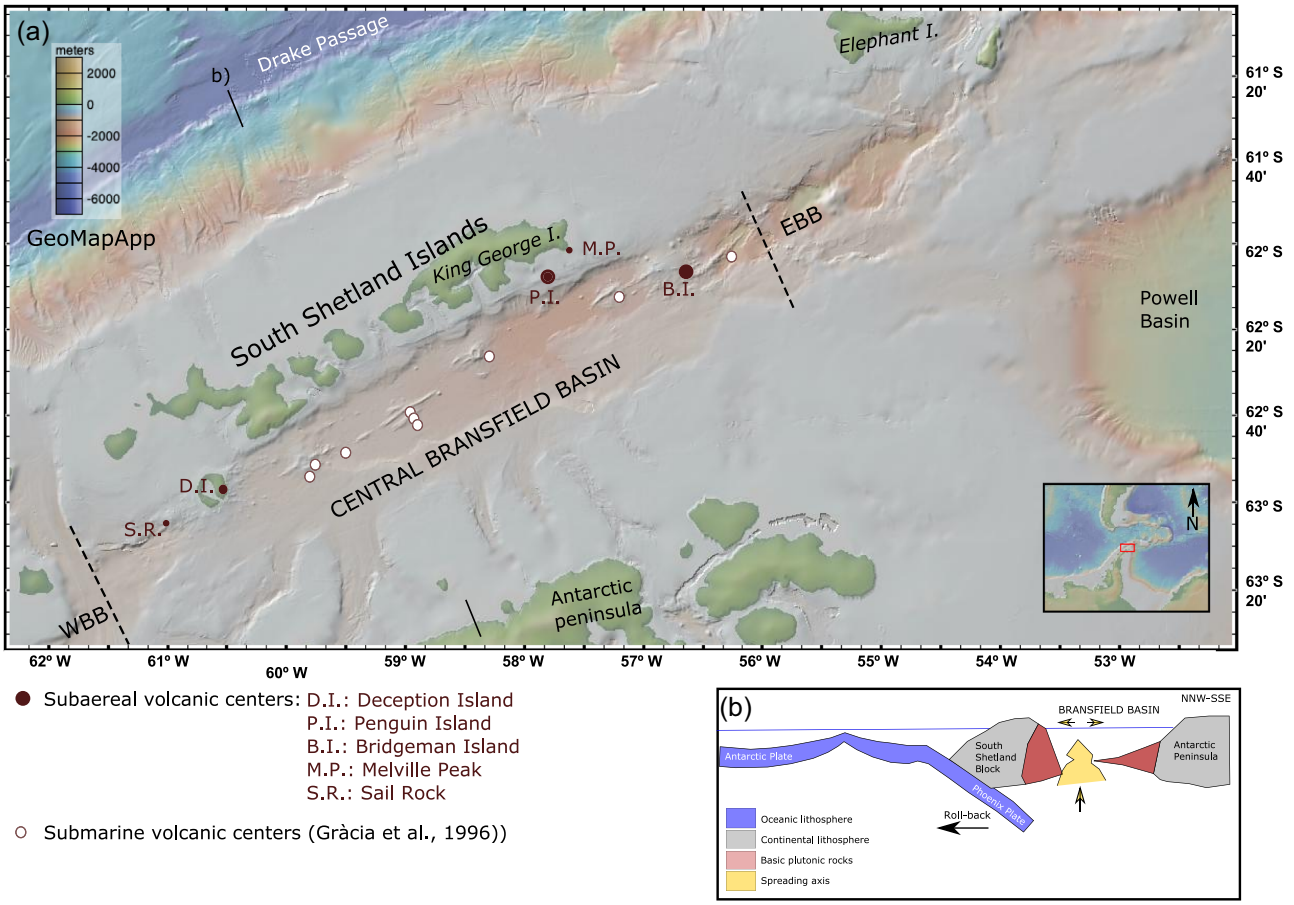

Figure 2. (a) Location of the volcanic centres in the Bransfield Basin (base map: GeoMapApp: http://www.geomapapp.org) (after Gràcia *et al.* 1996). EBB, East Bransfield Basin; WBB, West Bransfield Basin. (b) Schematic representation of the marked section, simplified from Galindo-Zaldívar *et al.* 2006).

of 180 m above sea level (a.s.l.) and 350 m wide crater containing a basaltic plug and radial dykes), with a second vent (Petrel Crater) formed ∼100 yr ago (Pańczyk & Nawrocki 2011). The oldest sequence of basaltic lava flows (low-potassium, calc-alkaline sequence) (Marr Point Fm) (Birkenmajer 1980), was dated with ^{40}Ar–^{39}Ar, which gives an estimate age of 2.7 ± 0.2 Ma (Pańczyk & Nawrocki 2011). Ages from Deacon Peak and Petrel Crater were obtained by lichenometry, which gives an estimate age of ∼300 yr for the former and ∼100 yr for the latter (Birkenmajer 1979).

Bridgeman Island measures 900 by 600 m and reaches a height of 240 m a.s.l. (Kraus *et al.* 2013). Birkenmajer (1994) defined this volcanic centre as a Late Pleistocene–Holocene stratovolcano over a submarine platform. Now it is an inactive volcanic remnant of a much larger volcanic edifice, eroded and submerged (as Sail Rock). Some fumarole activity was described during the 19th century (Gonza´lez-Ferra´n & Katsui 1970 as compiled in Kraus *et al.* 2013). Large parts of the island are composed of unconsolidated, red tephra (Kraus *et al.* 2013) (Fig. 3).

Geochemical information from Kraus *et al.* (2013, and references therein), which is based on major, trace, rare earth elements and isotopic composition, indicates similarities between the volcanic edifices of Bridgeman Island and Melville Peak, whereas Penguin Island is more similar to Deception Island and Sail Rock. Bridgeman Island shows a wide compositional range between basaltic andesite and dacite, whereas Penguin Island shows a narrow compositional distribution that classifies as basalt in the total alkali vs silica (TAS) diagram (Kraus *et al.* 2013). These authors found geochemical fingerprints for eruptions of the volcanic edifices that relate to tephra layers found elsewhere. In summary, Melville Peak and Bridgeman Island show Nb/Y ratios lower than 0.1 and Th/Nb ratios larger than 1.2, whereas Deception and Penguin islands have Nb/Y ratios between 0.1 and 0.3 and Th/Nb ratios lower than 0.5 (Kraus *et al.* 2013).

2.1 Sampling location

Seven sites were sampled in basaltic andesite–dacite lavas from Bridgeman Island (Fig. 3). The thickness of the lavas range from 0.5 to 3 m. On Penguin Island, samples were taken in two pyroclastic sites of the scoria cone (in bombs, since matrix was not possible to sample), three sites were taken in magmatic domes and plugs and two sites in the basaltic plateau lavas of ∼2.5 m in thickness (Fig. 4) with equally elongated vesicules on top of each lava flow. Flow direction on Bridgeman Island is assumed to originate in the centre and it is unknown for the plateau lavas. The volcanic material in the plug of Penguin Island most probably flowed upwards.

3 METHODOLOGY

All sites, except PI-5, were sampled with a gasoline powered drill, cooled with water. PI-5 was sampled by oriented blocks. A total of 8–13 cores were taken at each drilled location and oriented with a magnetic compass and clinometer (sun compass was not possible to use). Magnetic compass showed no deviation of the magnetized needle when approaching sampled site rocks. Magnetic declination correction of subtracting 10° was done in the laboratory. Due to time limitation, lavas were usually sampled in the centre of the flow, except in the lavas of Penguin Island, where drilled samples were taken continuously from the bottom to the top of the two plateau flows.

Cores were cut to standard palaeomagnetic samples (cylinders of 2.1 cm height, or cubes of 2 cm side for PI-5) obtaining between 12 and 36 standard samples per site (Table 1), and measured for the anisotropy of magnetic susceptibility (AMS) or magnetic fabric in the Laboratory of the University of Zaragoza, Spain (Geotransfer Group-IUCA) with a KLY3S (AGICO Inc.) instrument.

Magnetic susceptibility (k) is the relationship between the acquired magnetization of a material under an applied magnetic field (k = magnetization/applied field). This property is usually anisotropic in a rock, and when measured in different directions, provides the AMS (Tarling & Hrouda 1993).

The AMS is a symmetric second rank tensor which is represented by an ellipsoid with three axes ($k_{min} \leq k_{int} \leq k_{max}$), and defined by different magnetic parameters and the orientation of the axes. The most common magnetic parameters are L (k_{max}/k_{int}) and F(k_{int}/k_{min}), the corrected anisotropy degree (Pj, a measurement of how far from the sphere is the ellipsoid) and the shape parameter (T), being $T = (2n_2 - n_1 - n_3)/(n_1 - n_3)$, where $n_1 = \ln k_{max}$, $n_2 = \ln k_{int}$, $n_3 = \ln k_{min}$. Shapes range from oblate (pancake shape, planar fabric) when $+1 \geq T \geq 0$, to prolate (cigar shape, linear fabric) when $-1 \leq T \leq 0$ (Jelinek 1981). Magnetic parameters and orientation of the magnetic axes were calculated with the Anisoft software (Anisoft 4.2, Chadima & Jelinek 2008).

At room temperature the AMS mostly depends on the crystallographic preferred orientation, shape of grains, composition and sometimes, on the distribution-interaction of magnetic minerals (Tarling & Hrouda 1993), that is the magnetic fabric describes the orientation distribution of the magnetic carriers (Borradaile & Jackson 2004, and references therein).

Low temperature subfabric, that is measurements of the AMS on cooled samples in liquid nitrogen (77 K), were also obtained with the same instrument (KLY3S). At low temperature (77 K) the paramagnetic susceptibility is enhanced following the Curie–Weiss law [$Kp = C/T - \theta$; Kp is the paramagnetic susceptibility which increases with decreasing temperature—T. C is a constant and θ is the paramagnetic Curie temperature (T_c). In a perfect paramagnetic material the magnetic susceptibility at low temperature will be 3.8 times higher than at room temperature (Ihmlé *et al.* 1989). Three to six samples of seven selected sites were immersed in liquid nitrogen and cooled down for 1 hour before the first measurement position was taken, and between changes of measurement positions (three changes in KLY3S), they were kept for 10 min immersed in liquid nitrogen (*cf.* in Lüneburg *et al.* 1999).

Rock magnetic analyses as temperature dependence of the magnetic susceptibility, temperature dependence of the induced magnetization, acquisition of the isothermal remanent magnetization (IRM), remanence coercivity, and hysteresis loops were performed in order to identify the main carrier(s) of the magnetic fabric. Powdered samples of ∼200–500 mg were analysed. Thermomagnetic curves measuring the variation of the magnetic susceptibility with temperature (from room temperature to 700 °C) allows obtaining information about the percentage of paramagnetic material (with respect to ferromagnetic (s.l.) material) following a hyperbolic decay of the susceptibility with temperature (Petrovský & Kapička 2006). The temperature at which the final decay of the magnetic susceptibility occurs (Curie temperature for, i.e. magnetite, Néel temperature for, i.e. hematite), indicates the ferromagnetic (s.l.) mineral present, since the temperature transition of the ferromagnetic (s.l.) behaviour to paramagnetic behaviour is characteristic for every ferromagnetic (s.l.) mineral (Dunlop & Özdemir 1997). These analyses were carried out in the furnace of the KLY3S under an argon atmosphere to avoid mineral reactions during heating

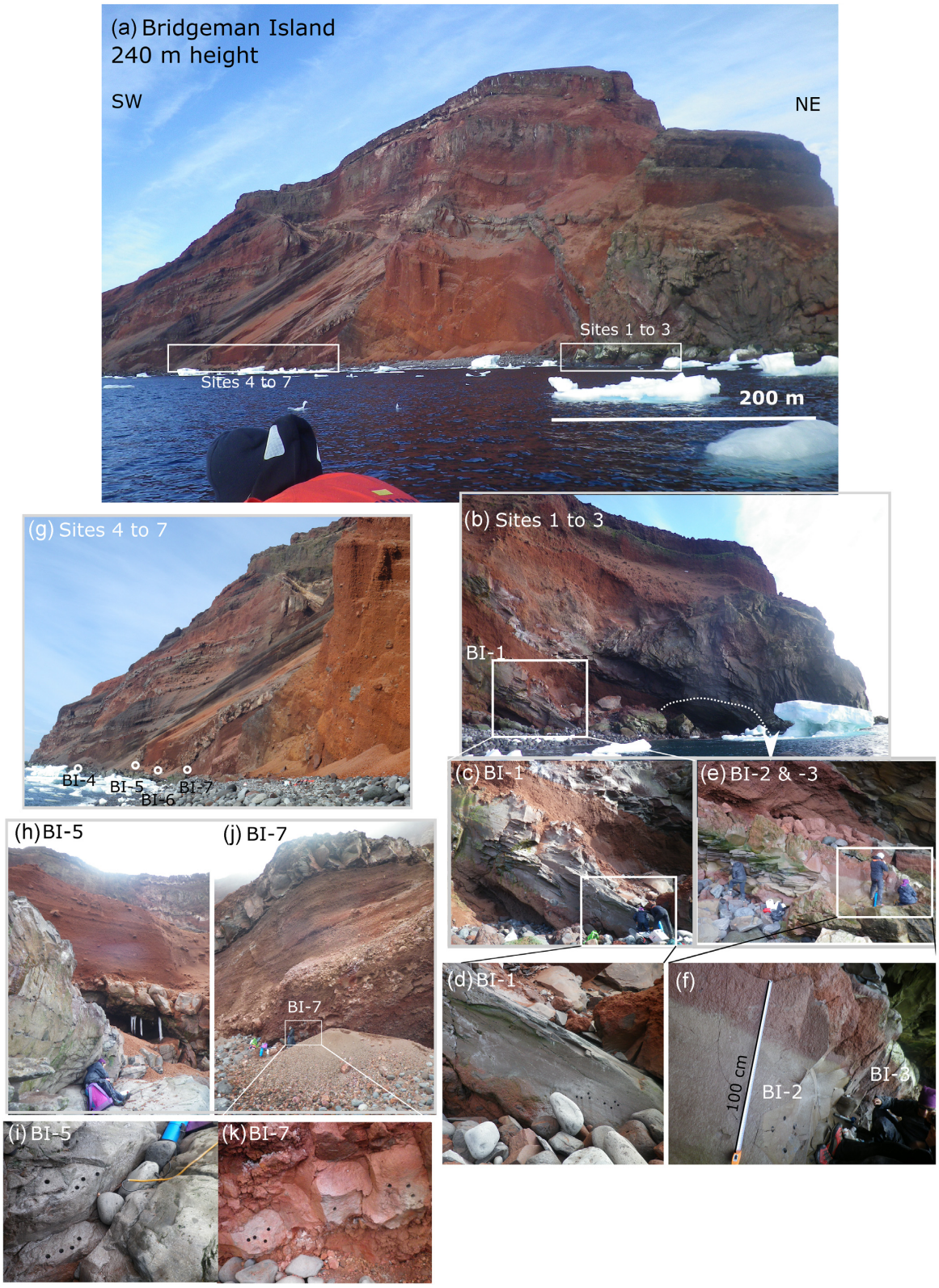

Figure 3. (a) Bridgeman Island and sampling areas. (b) Location of sites 1–3, at different scales of BI-1 (c and d), BI-2 and BI-3 (e and f). (g) Location of sites 4–7, with different zooming of BI-5 (h and i) and BI-7 (j and k).

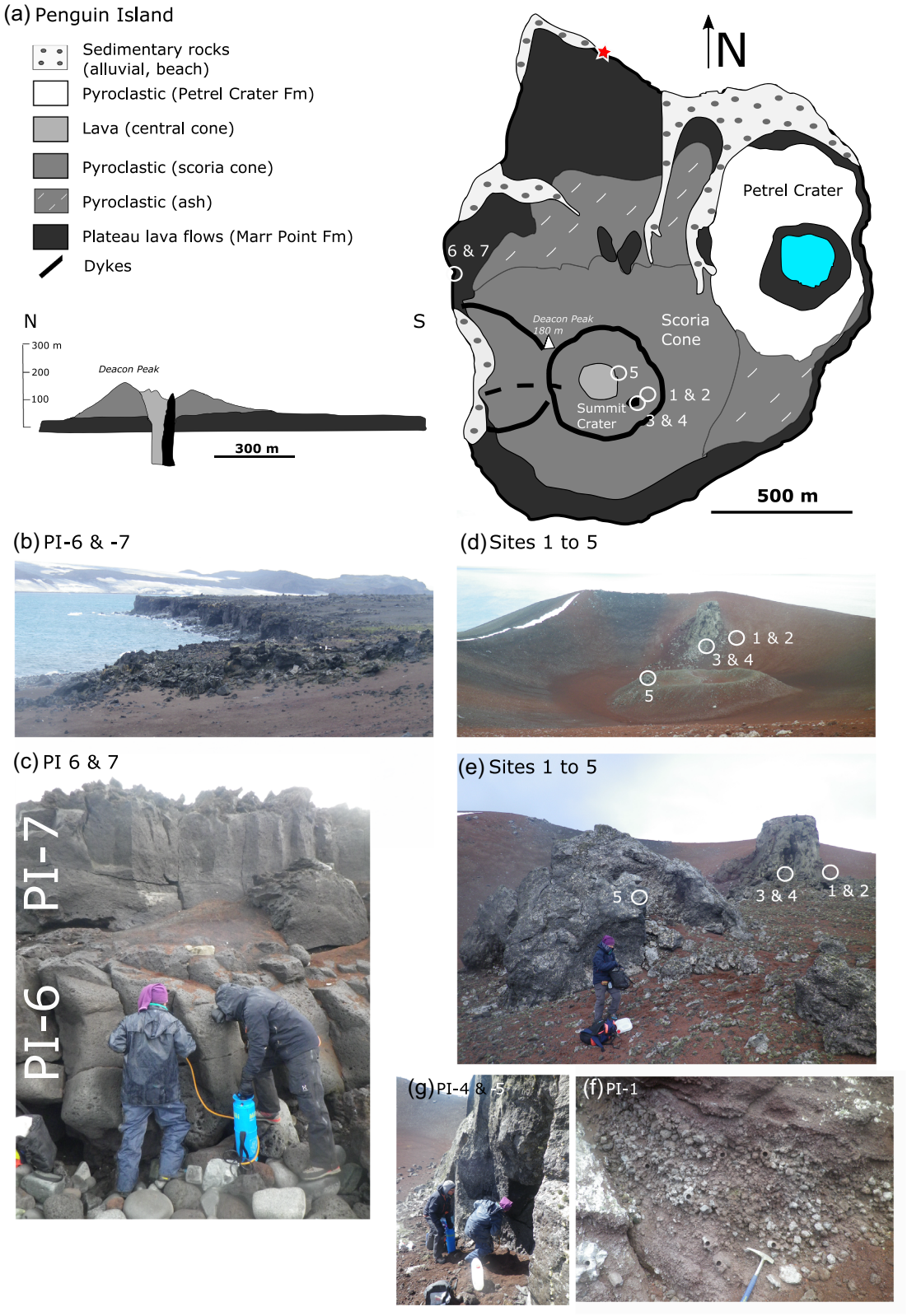

Figure 4. (a) Map and cross-section of Penguin Island (simplified from Pańczyk & Nawrocki 2011) and sampling sites (white circles). Red star locates the sampling for radiometric ages of the Marr Point Fm (Pańczyk & Nawrocki 2011). (b and c) Location of lava sites 6 and 7. (d and e) Different zooming of location of sites 1–5. (d) Picture near Deacon Peak looking to the SE. (f) Sampled bombs (PI-1). (g) Location of sites in the lava dome (PI-3 and PI-4).

Table 1. Parameters of the magnetic ellipsoid (AMS at room temperature): site, number of standard samples per site, averaged magnetic susceptibility (Km) in SI units (and standard deviation), *L*, *F* and their standard deviation, corrected anisotropy degree (*Pj*) and standard deviation and shape parameter *T* and standard deviation (calculated with Anisoft 4.2, Chadima & Jelinek 2008).

Site	*N* samples	Km	*SD*	L	*SD*	*F*	*SD*	*Pj*	*SD*	*T*	*SD*
BI-1	15	1.06E-02	9.56E-04	1.018	0.002	1.023	0.002	1.041	0.003	0.129	0.085
BI-2	12	9.89E-03	9.55E-04	1.012	0.002	1.020	0.004	1.032	0.005	0.249	0.113
BI-3	25	1.25E-02	1.62E-03	1.014	0.003	1.011	0.005	1.026	0.003	–0.147	0.302
BI-4	22	6.77E-03	1.20E-03	1.006	0.001	1.007	0.001	1.014	0.001	0.084	0.001
BI-5	16	1.50E-02	2.26E-03	1.007	0.002	1.012	0.002	1.019	0.002	0.252	0.157
BI-6	12	1.85E-02	2.48E-03	1.015	0.009	1.007	0.002	1.023	0.009	–0.246	0.333
BI-7	21	7.54E-03	1.24E-03	1.004	0.001	1.002	0.001	1.006	0.001	–0.250	0.269
PI-1	12	6.83E-03	3.66E-03	1.024	0.021	1.027	0.022	1.052	0.040	0.075	0.384
PI-2	12	1.05E-02	3.95E-03	1.016	0.025	1.014	0.010	1.032	0.031	0.087	0.380
PI-3	22	1.92E-02	3.90E-03	1.003	0.001	1.009	0.005	1.012	0.005	0.464	0.380
PI-4	20	1.82E-02	5.26E-03	1.002	0.001	1.010	0.004	1.013	0.004	0.591	0.004
PI-5	13	3.93E-02	6.03E-03	1.006	0.002	1.006	0.002	1.012	0.003	–0.009	0.426
PI-6	36	1.41E-02	3.19E-03	1.007	0.003	1.015	0.006	1.023	0.006	0.270	0.360
PI-7	25	9.54E-03	1.27E-03	1.008	0.003	1.011	0.004	1.020	0.005	0.146	0.260

and cooling, with ∼12 °C variation of temperature every minute. The Curie temperature (T_c) is calculated following the Petrovsky & Kapicka (2006) method, where the Curie temperature is that from which the inverse of the magnetic susceptibility follows the Curie–Weiss law; T_c is the lowest temperature end of a linear projection over a significant temperature range ('$1/\chi$ method', *cf*. Lattard *et al.* 2006). The determination of temperature is done in in Cureval8 software (AGICO Inc.) using the method by Petrovský & Kapička (2006).

In addition, other rock magnetic analyses were performed in the Curie Balance, the ultrasensitive variable field translation balance (MMAVFTB, Petersen Instruments) at the Palaeomagnetic Laboratory of the University of Burgos, Spain to determine: temperature dependence of the induced magnetization, acquisition of the isothermal remanent magnetization (IRM), remanence coercivity, and hysteresis loops. The final decay of the induced magnetization in the heating curve of the temperature dependence induce magnetization analyses also estimates the Curie (Néel) temperature (following Moskowitz 1981 or the second derivative calculations of the VFTB software package).

Observations under a Scanning Electron Microscopy (SEM) were performed in 3 gold-covered thin sections. Visual and backscattered X-ray analyses were performed using a Hitachi S-300CN at the Interdepartmental Research Service (SIdI) of the Universidad Autónoma de Madrid, Spain. The polished thin sections were prepared at the General Service of Research Support (SAI) of the University of Zaragoza in Spain.

4 RESULTS

4.1 Magnetic fabric at room temperature

The average of the magnetic susceptibility at room temperature per site ranges from 6.77 e-3 SI (BI-4) to 3.9 e-2 SI (PI-5) (Fig. 5 and Table 1). *L* and *F* values, as the shape parameter *T* indicates that oblate shapes of the magnetic ellipsoid dominate in both islands, although in Bridgeman Island, prolate shapes are also present at three sites (BI-3, 6 and 7). The closer values to zero in the *T* values indicate that the ellipsoid is neutral, which includes the spherical shape (slightly oblate shapes for positive values, or slightly prolate shapes, for negative values). *L* ranges from 1.002 (PI-4) to 1.024 (PI-1), *F* ranges from 1.002 (BI-7) to 1.027 (PI-1), whereas *Pj* ranges from 1.006 (BI-7) to 1.052 (PI-1) and *T* ranges from −0.250 (BI-7) to 0.591 (PI-4) (Fig. 5 and Table 1).

The stereographic projection of every site in Bridgeman Island (Fig. 6 and Table 2) reveals that all axes are well clustered. In addition, the magnetic lineation (k_{max} axes) does not cluster on the lava flow plane (except for sites 5 and 6). Magnetic lineation is found imbricated respect to the lava flow plane and in general terms, the magnetic lineation clusters following the same direction of the maximum dip of the lava flow plane, which varies between 35° and 10°, and the minimum axes cluster close to the pole of the lava flow plane (except in BI-3 and BI-4). Interestingly, between BI-2 and BI-3, which are located in the same lava flow, there is an interchange of intermediate and minimum axes with a change in the shape of the magnetic ellipsoid, from oblate (BI-2) to prolate (BI-3). As seen in Fig. 3, BI-3 shows a reddish coloration.

On Penguin Island the two sampled plateau lavas have subhorizontal planes (Figs 4b and c). Samples were taken along a vertical profile in the lavas. For an oblate magnetic ellipsoid, the magnetic lineation clusters in a NW–SE direction, close to the horizontal plane, whereas the pole to the magnetic foliation (k_{min} axes) clusters near a vertical direction (Fig. 7a). Near the top of the two plateau lavas, vesicles are more abundant; some samples in this part reveal a slightly imbricated magnetic fabric (k_{max} axes tilted and k_{min} axes not at the vertical position), more clearly at the top of PI-7 (scoriaceous), see top of Fig. 4(c).

The magnetic fabric in the volcanic domes and plugs shows a girdle distribution of k_{max} and k_{int} axes on a plane slightly tilted towards the NE (Fig. 7b). Finally, the magnetic fabric of the bombs (centimetric in PI-1 and decimetric in PI-2) sampled in the scoria cone of the summit crater shows a disordered distribution, as expected in pyroclastic deposits (Fig. 7c).

4.2 Magnetic fabric at low temperature

4.2.1 Bulk magnetic susceptibility at low temperature

The low temperature (LT) magnetic susceptibility increases moderately with respect to the room temperature (RT) magnetic susceptibility AMS: less than 1.5 (Fig. 8), and in two samples from PI-3 and site PI-5 there is a decrease (LT/RT ratio less than 1) suggesting that

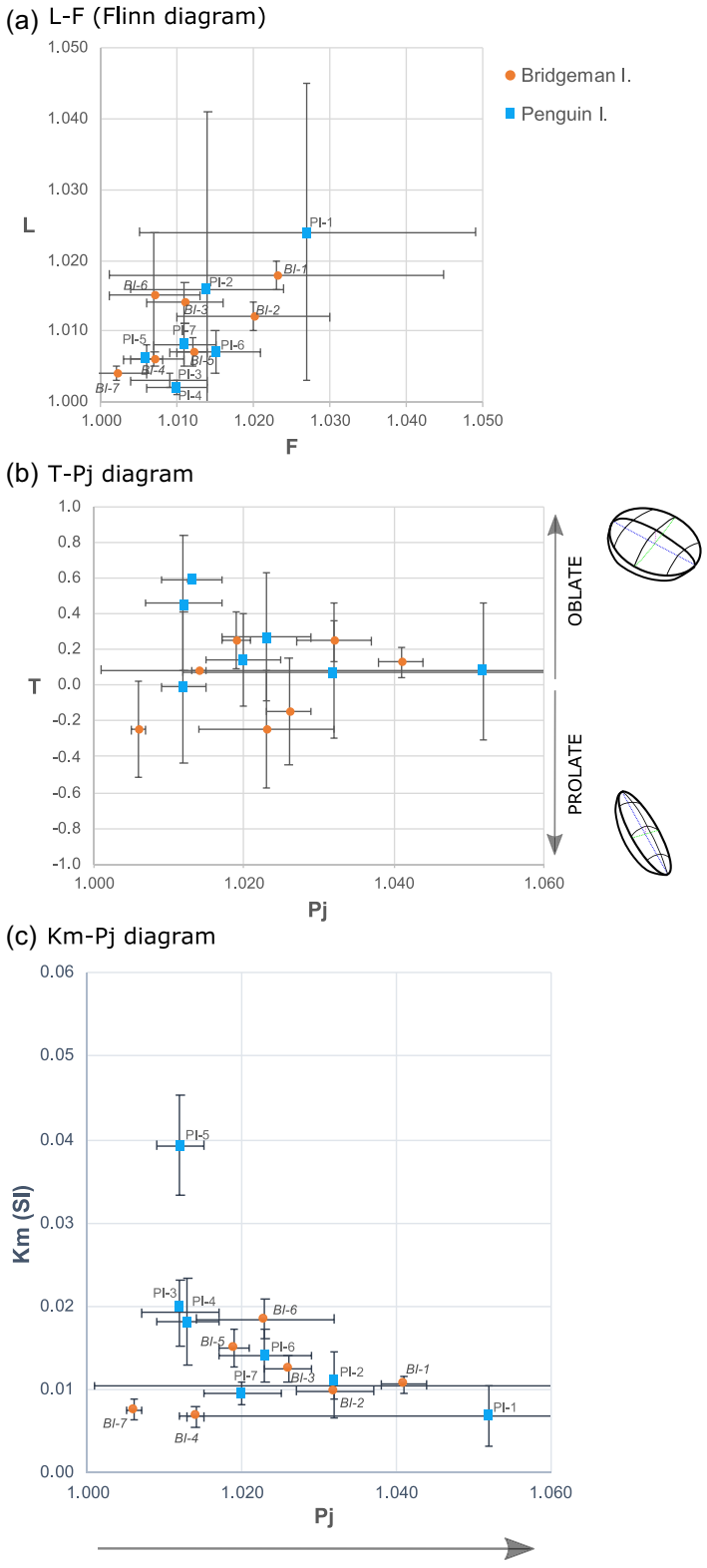

Figure 5. Magnetic parameters (average and standard deviation per site) of the two sampled islands. (a) Flinn diagram (*L* and *F* parameters). (b) Shape parameter (*T*)-Corrected anisotropy degree (*Pj*) diagram. (c) Bulk magnetic susceptibility (Km in SI)-Corrected anisotropy degree (*Pj*) diagram.

AMS is carried mostly by ferromagnetic (s.l.) minerals (i.e. magnetite, Ti-magnetite) with an influence of paramagnetic minerals (i.e. olivine, pyroxene). A high contribution of diamagnetic minerals (i.e. plagioclase) to the AMS is discarded since diamagnetic susceptibility does not vary with temperature (Tarling & Hrouda 1993). Therefore if paramagnetic minerals were the main carriers, the increase at LT of the bulk magnetic susceptibility should be higher than the constant contribution of diamagnetic minerals

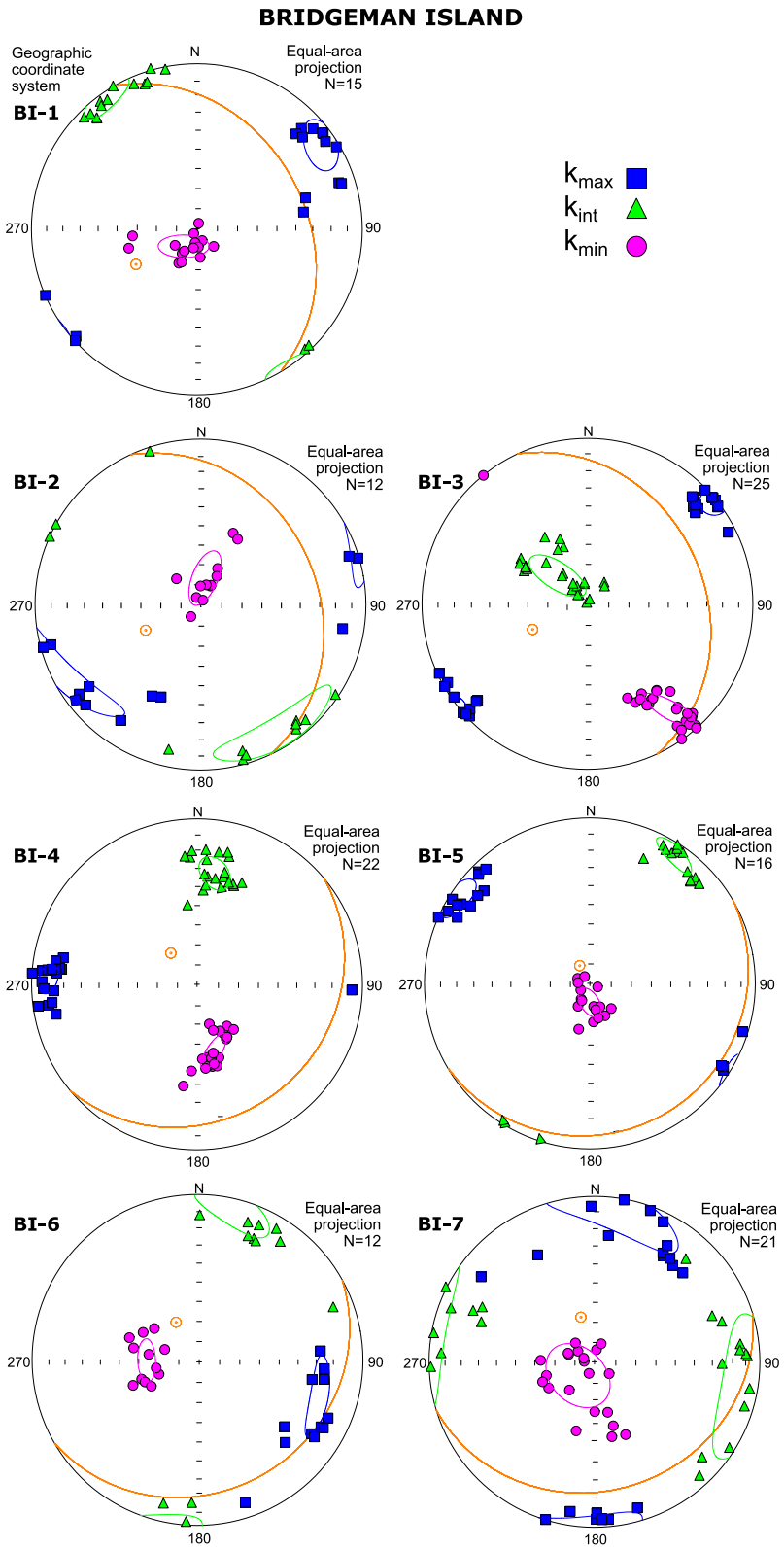

Figure 6. Lower hemisphere stereographic projection of the magnetic axes in each site of Bridgeman Island. The orange great circle is the projection of the lava plane and the orange small circle represent the pole to the lava flow plane.

Table 2. Orientation of the magnetic ellipsoid axes and confidence angles [declination (D) and inclination (I) in geographic coordinates] (Anisoft 4.2. software).

Site	k_{max} (D/I)	conf. angle	k_{int} (D/I)	conf. angle	k_{min} (D/I)	conf. angle
BI-1	55.9/10.1	11.5/8.9	325.3/3.3	10.8/7.	217.6/79.4	12.5/5.6
BI-2	240.1/8.5	27.3/7.3	148.6/10.1	26.2/9.5	18.5/76.7	14.3/6.2
BI-3	51.2/3	8.3/4.8	313.1/69.7	16.3/6.6	142.3/20	16/3.8
BI-4	272.1/10.8	6.7/5	9/32.4	9.5/6.2	166/55.4	10.1/3.6
BI-5	302.4/5	9.2/6.8	33.1/8	9/5.1	180.6/80.6	7.9/4.5
BI-6	106.4/24.7	17.3/5.2	13.5/6.1	17.6/9.3	270.6/64.5	10.4/4.4
BI-7	9/8.1	28.5/12.2	100/6.9	27.7/16.1	230.1/79.3	17.8/13.3
PI-1	119.7/21.3	73.8/20.4	211.9/5.4	73.8/33.4	315.4/67.9	33.7/20.9
PI-2	337/54.1	66.4/31.9	123.8/31.2	80/50.2	223.7/15.9	80/59.4
PI-3	46.9/40.3	24/7.1	137.7/0.9	24/14.7	228.7/49.7	14.9/6.9
PI-4	83.7/20.5	17.2/7	340.3/31.8	18.8/12.6	200.8/50.7	16/4.1
PI-5	177/20.4	15.3/11.5	80.2/17.5	28.4/13.5	312.8/62.6	29.7/7.8
PI-6	163.7/13	32.4/10.8	68.6/20.8	32.5/17.1	283.6/65.2	17.4/10.6
PI-7	125.8/3.1	25.7/17.7	215.8/0.4	21.4/13.2	312.6/86.9	23.7/11.5

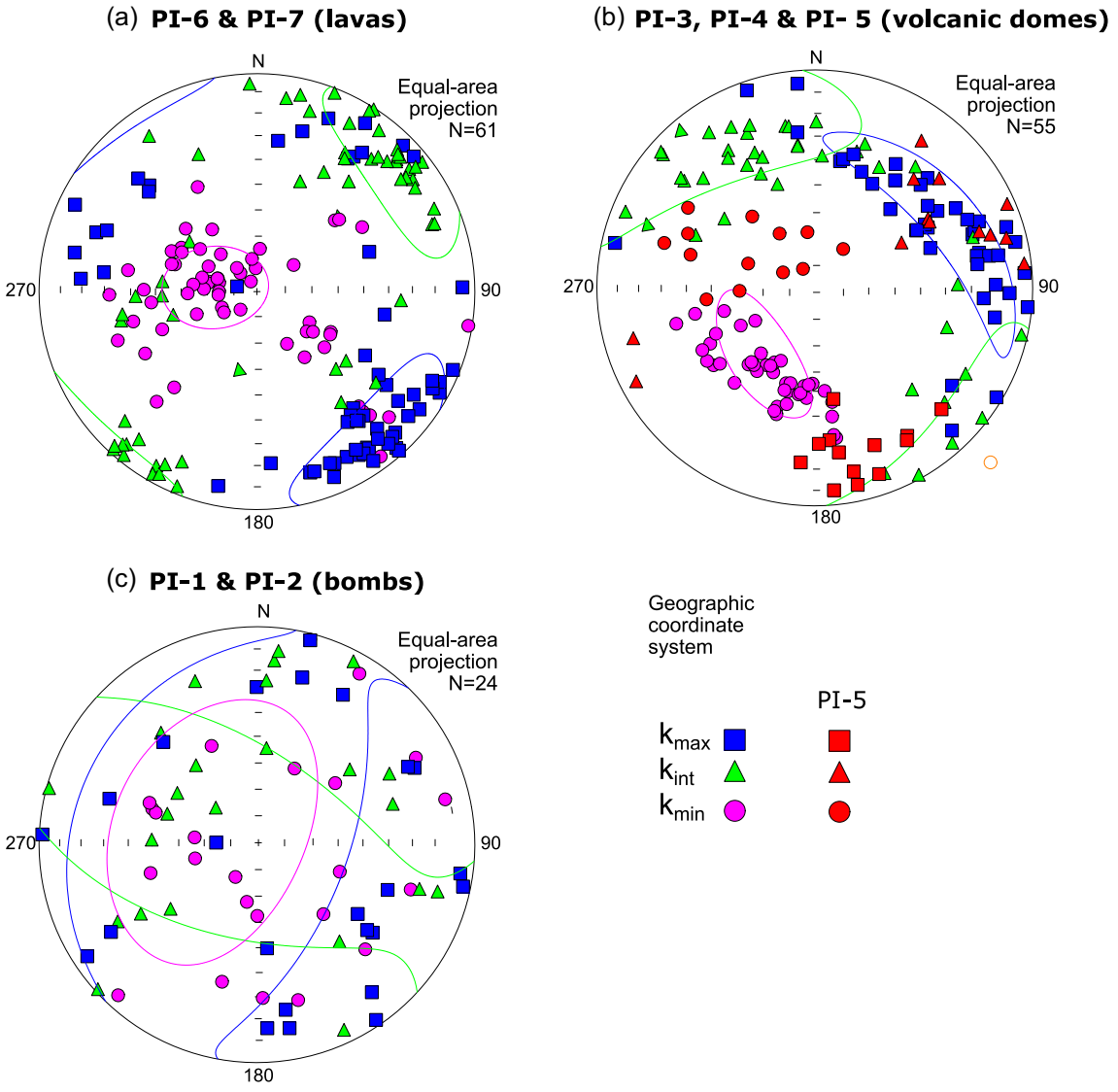

Figure 7. Lower hemisphere stereographic projection of the magnetic axes in each site of Penguin Island. Sites are grouped depending on the magmatic material, (a) lava, (b) dome and (c) bombs of the pyroclastic deposits in the summit scoria cone.

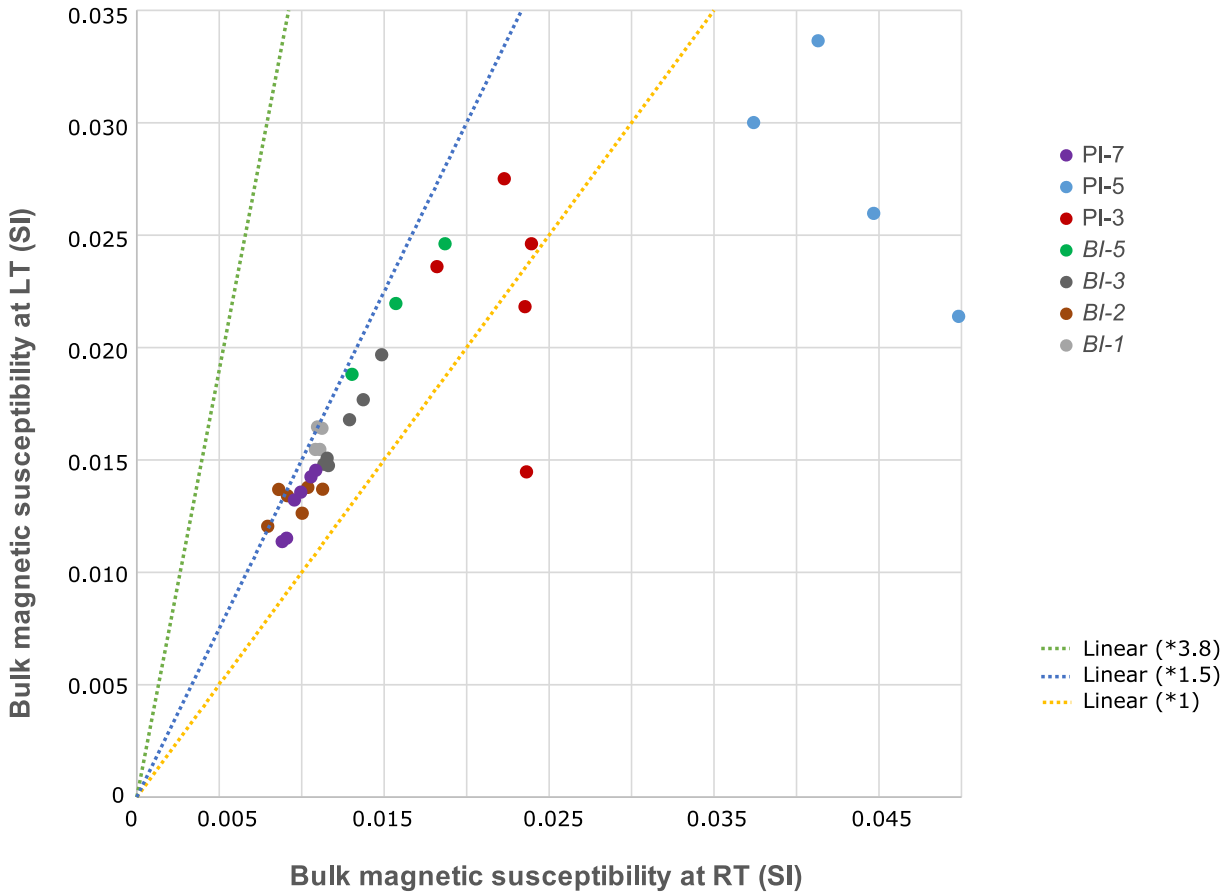

Figure 8: Magnetic susceptibility at room temperature (RT), horizontal axis and at low temperature (LT), vertical axis.

which it is not shown in the results of Fig. 8 (Biedermann *et al.* 2014, 2015, 2016). In addition, the magnetic susceptibility of these diamagnetic minerals is weak when compared to other rock forming minerals; 1.53×10^{-9} m^3 kg^{-1} (Biedermann *et al.* 2016, and references therein).

4.2.2 Magnetic fabric at low temperature

The orientation of the magnetic fabric at low temperature is similar to the one at room temperature or more scattered (as in PI-3) suggesting that paramagnetic minerals share the orientation of the magnetic fabric at room temperature (Fig. 9 and Table 3).

4.3 Rock magnetic analyses: magnetic carrier(s) and interpretation

4.3.1 Thermomagnetic curves (KLY3S)

The thermomagnetic curves analysed in the KLY3S [magnetic susceptibility (k) versus temperature, Figs 10 and 11] are not completely reversible, indicating that the ferromagnetic mineral is not stable during the measurements (not stoichiometric) although BI-1, BI-3 and PI-6 show the most reversible behaviour. The final decay of the magnetic susceptibility in the heating curve coincides with the increase of the magnetic susceptibility in the cooling curve around 580–606 °C (Table 4) except in BI-6, where the increase of the magnetic susceptibility in the cooling curve occurs at a lower temperature than the final decay of the magnetic susceptibility in the heating curve, and it is slightly smaller in BI-4. All curves show higher magnetic susceptibilities after the procedure except for BI6. Samples BI-1, BI-3 and PI-6 show the most reversible behaviour (see factor A_{50} Table 4), adapted from the alteration numerical approach of Hrouda (2003) where $A_{50} = 100 \times (k_{50} - K_{50})/K_{50}$; being k_{50} (K_{50}) the magnetic susceptibility at 50 °C in the cooling (heating) curve respectively. However, in BI-6 and PI-4 the maximum differences of magnetic susceptibility between the heating and cooling curves do not occur at 50 °C but at higher temperatures, at 564 and 410 °C, respectively (shown in brackets in Table 4).

These curves allow determining the ferromagnetic mineral present due to the magnetic ordering that changes to a paramagnetic behaviour at a certain temperature (Curie for ferrimagnetic minerals, i.e. magnetite- or Néel -for antiferromagnetic minerals, i.e. hematite-), which is different for every ferromagnetic (s.l.) mineral. The Tc is very sensitive to the Ti content on the iron-oxides (Lattard *et al.* 2006) the level of oxidation and the level of impurities present, therefore lowering the T_c as the content of Ti and impurities or the oxidation level increases (Dunlop & Özdemir 1997).

The calculated T_c is 580–606 °C, close to the T_c of Ti-poor magnetite (580 °C), Ti-poor maghemite (formed for example due to low temperature oxidation of magnetite) or Ti-hematite. In addition, the curves do not show paramagnetic behaviour, that is they do not show a hyperbolic decay on the heating curve. Some heating curves show a narrow increase before the final decay (Hopkinson peak) at the T_c (i.e. BI-1, BI-2, BI-3, BI-6, PI-6 and PI-7 samples). The Hopkinson peak flanks other phase transition such as the Verwey

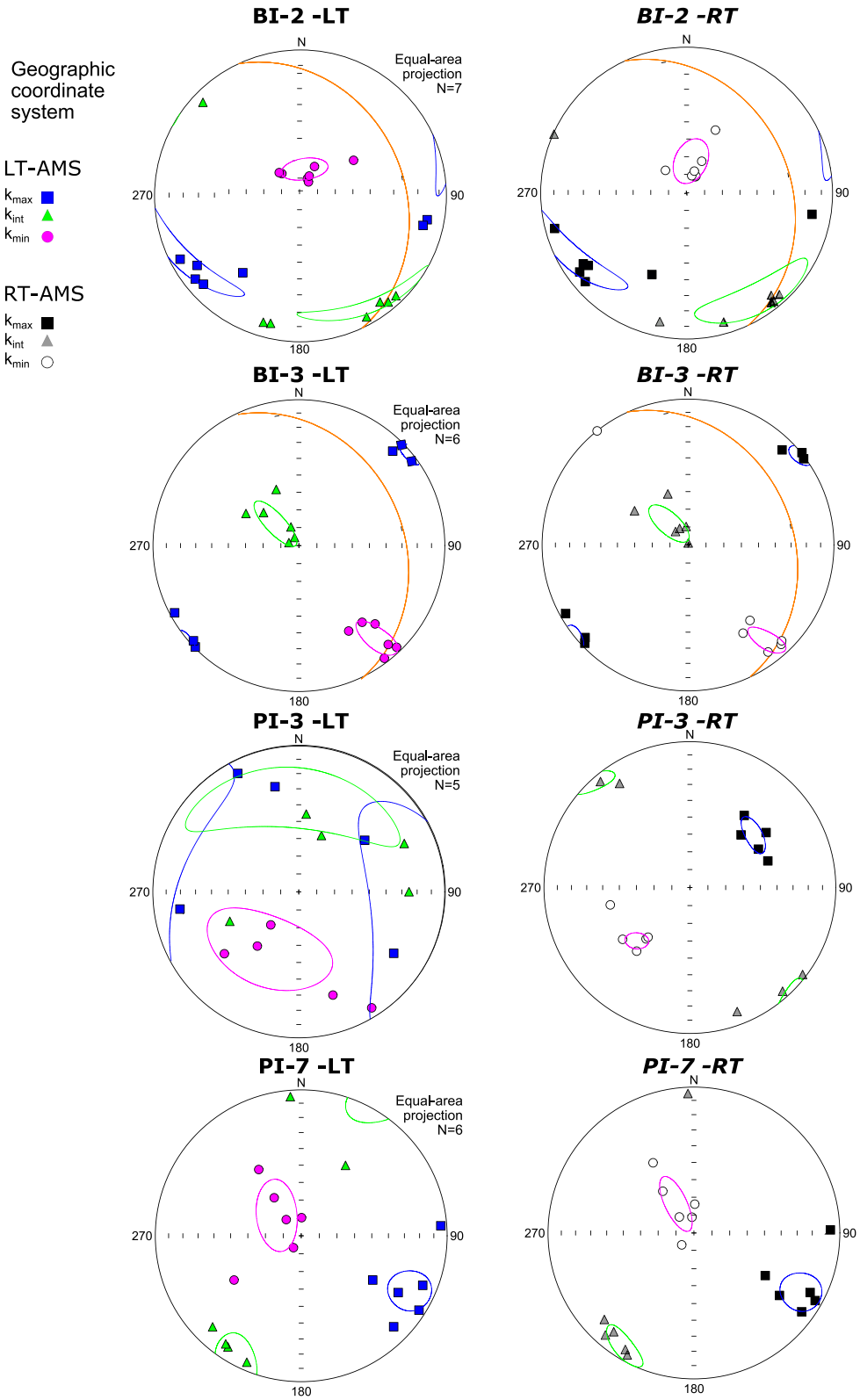

Figure 9. Lower hemisphere stereographic projection in geographic coordinates of selected sites of the magnetic fabric at low temperature (left-hand side), and the same samples at room temperature (right-hand side) for comparison. The orange circle for the BI sites is the projection of the lava plane.

transition of magnetite at low temperature (T_v: 110–120 K = ∼ −153 to ∼ −163 °C), this transition occurs as magnetite transforms from monoclinic to cubic spinel structure. T_v can vary with the Ti content and oxidation level as the T_c does (Özdemir *et al.* 1993; Dunlop & Özdemir 1997). The height of the Hopkinson peak before the Curie point is related to the grain size of magnetite (narrower and larger for smaller grains and no peak for larger grains; Dunlop 2014, and references therein).

Table 3. Magnetic fabric parameters and orientation of axes in sites measured at low temperature (LT) and the same samples at room temperature (RT). Legend as in Tables 1 and 2. When confidence angles (conf. ang.) cannot be calculated, mean vector with α_{95} is.

Site	N samples	Km	*SD*	*L*	*SD*	F	*SD*	*Pj*	*SD*	*T*	*SD*	k_{max}	conf. ang. (α_{95})	k_{int}	conf. ang. (α_{95})	k_{min}	conf. ang. (α_{95})
PI-7-LT	6	1.31E-02	1.26E-03	1.012	0.006	1.012	0.003	1.024	0.008	0.048	0.307	117/18	15.1/9.1	208/4	18/9.2	309/71	20.3/11.3
PI-7-RT	6	9.80E-03	8.05E-04	1.010	0.004	1.009	0.002	1.019	0.004	0.000	0.250	118/16	14.7/8.5	211/9	12.6/6.1	330/71	17.0/6.0
PI-3-LT	5	2.24E-02	4.89E-03	1.010	0.007	1.014	0.009	1.025	0.012	0.174	0.519	99/15	57.6/32.2	358/35	57.5/18.8	208/51	35.2/20.9
PI-3-RT	5	2.23E-02	2.39E-03	1.002	0.001	1.010	0.006	1.014	0.006	0.546	0.365	50/43	10.5/5.1	318/3	10.1/5.2	235/47	6.6/4.4
PI-5-LT	4	2.78E-02	5.28E-03	1.010	0.005	1.017	0.006	1.027	0.009	0.270	0.290	30/43	67.5	210/66	—	0/83	—
PI-5-RT	4	4.33E-02	5.27E-03	1.005	0.002	1.004	0.002	1.010	0.001	-0.037	0.467	170/20	11.7	71/22	15.9	297/60	20
BI-2-LT	6	1.33E-02	7.06E-04	1.015	0.002	1.018	0.003	1.031	0.004	0.198	0.104	241/10	29.9/6.9	149/13	28.7/11.6	6/74	14.4/8.5
BI-2-RT	6	9.79E-03	9.62E-04	1.015	0.002	1.023	0.002	1.038	0.002	0.216	0.002	151/9	33.1/6.4	150/12	32.2/4.4	9/75	13/6
BI-3-LT	6	1.65E-02	1.99E-03	1.022	0.006	1.015	0.006	1.039	0.003	-0.182	0.279	49/2	6/4.3	313/71	16.8/5.4	140/19	16.8/4.9
BI-3-RT	6	1.22E-02	1.71E-03	1.014	0.003	1.011	0.005	1.025	0.003	-0.159	0.341	51/1.3	6.4/1.3	316/74	14.2/6	141/16	14.3/4
BI-5-LT	3	2.18E-02	2.91E-03	1.008	0.001	1.017	0.004	1.026	0.005	0.284	0.107	305/11	9.5	35/7	9.9	160/77	12.7
BI-5-RT	3	1.58E-02	2.82E-03	1.007	0.001	1.013	0.002	1.020	0.002	0.323	0.096	306/10	13.4	38/8	11.5	165/78	12.6
BI-1-LT	4	1.60E-02	5.61E-04	1.023	0.003	1.028	0.003	1.052	0.002	0.082	0.095	73/20	—	332/5	17	224/81	21.8
BI-1-RT	4	1.10E-02	1.72E-04	1.018	0.002	1.024	0.002	1.043	0.002	0.137	0.093	72/21	—	330/5	16.1	8/86	24.7

Some heating curves also show a decay of the magnetic susceptibility around 400–450 °C, suggesting the presence of another mineral phase (i.e. Ti-rich magnetite), see BI-1, BI-2, (BI-3 weak), BI-6, PI-5, PI-6 and PI-7 samples (Figs 10 and 11). The samples from the pyroclastic material (PI-1 and PI-2) show a distinct behaviour, with two magnetic phases in the heating and cooling curves, with higher temperature decays in PI-7 than in PI-6 (Figs 10 and 11, and Table 4).

The low temperature curves (light blue curves in Figs 10 and 11) indicate the presence of Ti-poor magnetite in BI-7, BI-2 and PI-4, with a Verwey transition (T_v) at −152, −166 and −158 °C, respectively. The lowering of the T_v in BI-3 (−172 °C), PI-6 (−176 °C) and PI-7 (−170 °C) and its absence in BI-6 suggest higher Ti content, impurities or some oxidation level of the magnetite grains.

4.3.2 Thermomagnetic curves (Curie balance)

The temperature dependence induced magnetization curves of the Curie balance (VFTB) are more similar for all samples except in BI-6, PI-1 and PI-2 (Figs 10b and 11b). They show only one magnetic phase maybe due to the instrument lower measurement sensitivity (except in BI-6 and PI-1) relative to the temperature dependence magnetic susceptibility curves, as already seen in previous studies (Goguitchaichvili *et al.* 2001, and references therein). T_c in the heating curve is slightly higher than in the cooling curve, suggesting some mineralogical change during heating (on Ar atmosphere during the procedure), or due to some hysteresis in heating-cooling curves, that is during cooling, the sample is still at higher temperature than the temperature control—located out of the sample—and this can be also due do the cooling speed. T_c was calculated according to Moskowitz (1981) or the second derivative of the heating curve range from 470 to 600 °C (Table 4).

4.3.3 Isothermal remanent magnetization, coercitivity of remanence and hysteresis loops

The isothermal acquisition of the remanent magnetization curve (IRM, blue curve in Figs 10c and 11c) and coercitivity curve (orange curve in Figs 10c and 11c) together with the hysteresis loops show a 'soft' magnetic mineral present, with low coercitivity as in magnetite and maghemite. The B_{cr} from the hysteresis loop are all below 50 mT (except BI-7 and PI-7) as seen in the red line of Figs 10(c) and 11(c). The IRM curve saturates before 200 mT, except in samples PI-1 and PI-2 (bombs). The saturation before 200 mT supports the presence of a low coercitivity mineral. The hysteresis loops show the wasp-waisted shape only in sample PI1. This shape can be the result of the presence of different magnetic phases, magnetic grain sizes or magnetic anisotropy (Tauxe *et al.* 1996; Weil & Van der Voo 2002, and references therein).

The rock magnetic results indicate the presence of a low coercitivity magnetic mineral with T_c closer to Ti-poor magnetite (maghemite), and in some samples, Ti-rich magnetite (maghemite). The paramagnetic content is not relevant for the magnetic fabric.

4.4 SEM observations

4.4.1 Petrography via backscattered electron images and EDX

The main rock forming minerals are silicates: plagioclase, pyroxene (augite and/or diopside), olivine and minor K-feldspar (Fig. 12). Pyroxene and plagioclase phenocrysts occur in prismatic shapes with a range of grain sizes varying from 100 to 600 μm, and also forming the matrix with laths of lengths from 10 to 100 μm. Olivine grains are larger and more abundant in the Penguin Island sample (Figs 12e and f).

Iron oxides represent ∼5–10 per cent of the minerals and they appear in euhedral grains of 1–50 μm. Vermicular grains of elongated appearance of ∼5 μm length by less than 2 μm across are also observed. The vermicular forms of Ti-iron oxides are at the Ca-poor pyroxene reaction rim on olivine grains or on pyroxene grains (Figs 12b and c).

Euhedral grains show Ti rich lamellae related to oxidation at high temperature (deuteric oxidation) 600–1000 °C (Figs 12d, f and h). On cooling, a Ti–magnetite grain will produce first ilmenite lamellae within (Ti) magnetite as presented in McElhinny & McFadden (2000), since magnetite–ülvospinel intergrowths are rare in nature due to the presence of oxygen in the melt, therefore:

$$\underset{\text{(ulvospinel)}}{6Fe_2TiO_4} + O_2 = \underset{\text{(ilmenite)}}{6FeTiO_3} + \underset{\text{(magnetite)}}{2Fe_3O_4}$$

Low temperature oxidation (maghemitization) will produce cracks in the Ti–Fe oxides and little alteration below 200 °C. Maghemite is an unstable phase, and when heated inverts to hematite at temperature between 250 and 750 °C, with a Tc in the range 590–675 °C. The cracks are the result of the transformation into a cation deficient Ti–maghemite, with lattice parameters different from the original stoichiometric Ti–magnetite which strain the oxidized surface and therefore cracks (McElhinny & McFadden 2000).

Vanadium is found as an impurity in the Ti–Fe oxides of both islands and chromite (iron chromium oxide) with Mg and Al (and Ti) impurities in the sample from Penguin Island.

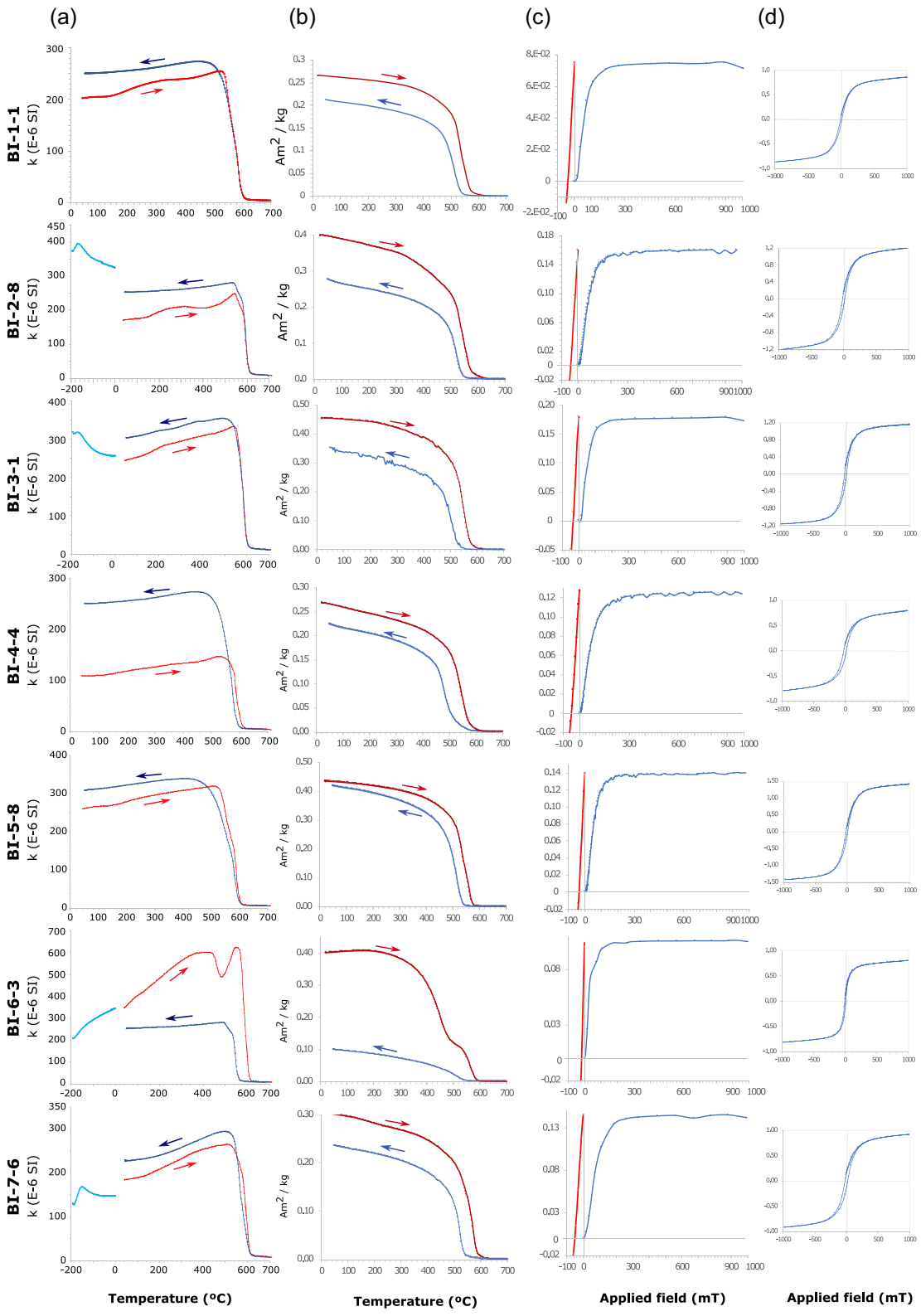

Figure 10. In Bridgeman Island: (a) Temperature dependence of magnetic susceptibility measured in the KLY3, red: heating curve, dark blue: cooling curve, light blue: heating from low temperature ~77 K to ~0 °C curve. (b) Temperature dependence of induced magnetization measured in the Curie Balance -VFTB-, heating curve: red, cooling curve: blue. (c) Acquisition of the Isothermal Remanent Magnetization (IRM) curve (blue) and backfield demagnetization curve (red) measured in the Curie balance. (d) Hysteresis loops (uncorrected for high field slope) measured in the Curie balance. Vertical axes in (c) and (d) have the same units as in (b).

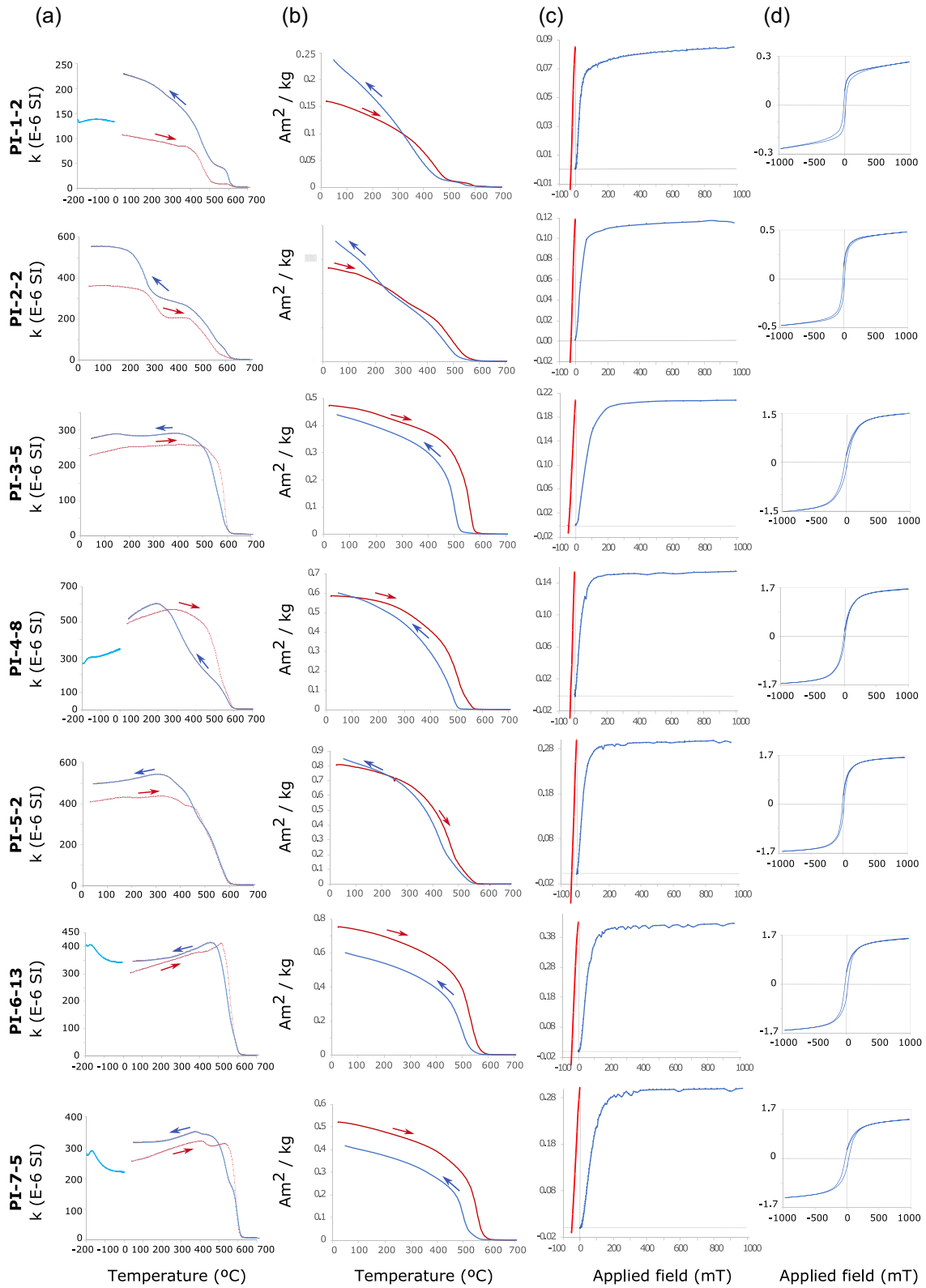

Figure 11. In Penguin Island: (a) Temperature dependence of magnetic susceptibility measured in the KLY3, red: heating curve, dark blue: cooling curve, light blue: heating from low temperature ∼77 K to ∼0 °C curve. (b) Temperature dependence of induced magnetization measured in the Curie Balance -VFTB-, heating curve: red, cooling curve: blue. (c) Acquisition of the Isothermal Remanent Magnetization (IRM) curve (blue) and backfield demagnetization curve (red) measured in the Curie balance. (d) Hysteresis loops (uncorrected for high field slope) measured in the Curie balance. Vertical axes in (c) and (d) have the same units as in (b).

Table 4. Rock magnetic analyses provide: Verwey temperature (in °C) (KLY3), Curie temperatures (in °C) calculated after the thermomagnetic heating curves (in the KLY3 and VFTB), numerical approximations to the alteration of the procedure (A_{50} and A_{max} in BI-6 and PI-4) and parameters obtained in the Curie balance (VFTB) from the corrected hysteresis loop: saturation remanence M_{rs}, saturation magnetization M_s, bulk coercitive field B_c and remanence coercitive field B_{cr}. When two temperatures are present in the same cell, two magnetic phases are present.

	KLY·Tv (°C)	KLY·Tc (°C)	*Reversivility* Hrouda (2003) $A_{50} = 100\ (k_{50} - K_{50})/K_{50}$; $A_x = 100\ (k_x - K_x)/K_{50}$	VFTB-T_c (°C) Moskowitz (1981)/Derivative	VFTB-corrected hysteresis loop $Am^2\ kg^{-1}$ M_s	$Am^2\ kg^{-1}$ M_{rs}	mT Bc	mT Bcr	M_{rs}/M_s	H_{cr}/H
BI-1-1	—	∼390 and 580	23.2	560	7.40E-04	7.89E-05	11.4	38.3	0.11	3.36
BI-2-8	−166	∼400 and 590	47.9	575	1.04E-03	1.65E-04	16.9	45.17	0.16	2.67
BI-3-1	−173	590	24.2	560	1.07E-03	1.86E-04	15.9	35.75	0.17	2.25
BI-4-4	—	594	131.5	564	6.44E-04	1.30E-04	21.01	49.2	0.20	2.34
BI-5-8	—	593	18.5	570	1.28E-03	1.45E-04	12.65	34.82	0.11	2.75
BI-6-3	NO	∼450 and 606	−28.9 (A564: −166.1)	500 and 578	7.15E-04	1.13E-04	7.6	17.7	0.16	2.33
BI-7-6	−152	600	23.7	580	8.01E-04	1.48E-04	21.58	51.51	0.18	2.39
PI										
PI-1-2	−100	460 and 597	114.7	470 and 600	2.04E-04	8.63E-05	14.89	26.36	0.42	1.77
PI-2-2	—	350 and 600	53.4	560	4.12E-04	1.21E-04	12.45	25.77	0.29	2.07
PI-3-5	—	590	20.7	570	1.33E-03	2.14E-04	19.64	46.42	0.16	2.36
PI-4-8	−158	580	5.3 (A410: −49.9)	560	1.48E-03	1.64E-04	9.27	26.78	0.11	2.89
PI-5-2	—	200, 400 and 584	20.7	574	1.51E-03	3.11E-04	12.19	30.73	0.21	2.52
PI-6-13	−173	∼400 and 583	13.2	565	1.42E-03	4.34E-04	24.42	40.79	0.31	1.67
PI-7-5	−170	440 and 594	23.4	575	1.18E-03	3.07E-04	27.27	50.56	0.26	1.85

5 DISCUSSION

5.1 Magnetic mineralogy

Ferromagnetic minerals are the main carriers of the magnetic fabric (AMS) when the value of magnetic susceptibility is high ($>10^{-3}$ SI) and the degree of anisotropy is >35 per cent (Rochette 1987). In our case study, the first condition is met (average of k varies from 6×10^{-3} to $3.9\ 10^{-2)}$) but not the second (average of *Pj* are between 0.6 and 5.2 per cent). The anisotropy of the magnetic fabric is low (low *Pj* values). This condition can arise from different factors depending on the minerals contributing to the magnetic fabric and their degree of alignment, that is if ferromagnetic minerals are the main carriers, it would suggest they are mostly isotropic, their alignment is weak or only a fraction of them contribute to the magnetic fabric, and then the magnetic fabric is influenced by the orientation distribution of paramagnetic minerals. This situation is not uncommon in igneous rocks were the main carriers of the magnetic fabric are certain grains of (Ti)-magnetite, as indicated by the anhysteretic anisotropy of the remanence (Raposo & Berquó 2008; Raposo 2020). Measurements in a torque magnetometer at room and low temperature can disentangle the main carrier of the magnetic anisotropy (Schmidt *et al.* 2007).

In this study, the magnetic properties and SEM observations suggest that the main carrier of the magnetic susceptibility are Ti-poor magnetites/maghemites, a composition that is anomalous for MORB, where iron oxides are Ti-rich ($x = 0.6$ with $T_c \sim 400$ °C, Lattard *et al.* 2006). However, in some sites an enriched Ti-magnetite may be present (*cf.* Figs 10 and 11).

Different grain sizes of Ti–Fe oxides have been observed in thin section, from euhedral grains up to 50 μm and vermicular grains up to 5 μm. The Tc higher than 580 °C indicates some level of oxidation to Ti-poor maghemite (Tc range from 590 to 675 °C, McElhinny & McFaden 2000). The Hopkinson peak in some of the thermomagnetic curves (*k*–*T* curves) suggests the predominance of small grains (SD). The value of the magnetic susceptibility (*k*) is similar to other basaltic rocks with interpreted low viscosity (Caballero-Miranda *et al.* 2016). Therefore, possible changes in the corrected degree of anisotropy will not be related to this viscosity factor [Hrouda *et al.* (2005) found that viscosity of magmas correlates with the degree of anisotropy].

Paramagnetic signal is considered to have a low contribution to the magnetic anisotropy of these igneous rocks, although silicates (plagioclase) may influence the growth of the Ti–Fe oxides (as seen in other basalts, Bascou *et al.* 2005). In other cases, magnetic grains are assumed to form as interstitial phase in pre-existing silicate grains (such as plagioclase, pyroxenes), particularly within interstitial glass forming globular aggregates (Fanjat *et al.* 2012, and references therein). On Bridgeman Island, vermicular Ti–Fe oxide grains are observed on the rim of olivine grains.

The saturation above 200 mT in the IRM acquisition curve suggests the presence of (Ti)–hematite (i.e. PI-1, Fig 11).

Therefore, SEM observations suggest that the main carrier(s) of the magnetic fabric at room temperature are a small fraction of ferromagnetic *s.l.* grains (Ti–Fe oxides) or almost isotropic ferromagnetic *s.l.* grains (Ti–Fe oxides) with contribution of paramagnetic minerals. The Ti–Fe oxides appear unoriented in the thin sections (except the vermicular grains in the olivine grains, where they have a radial distribution).

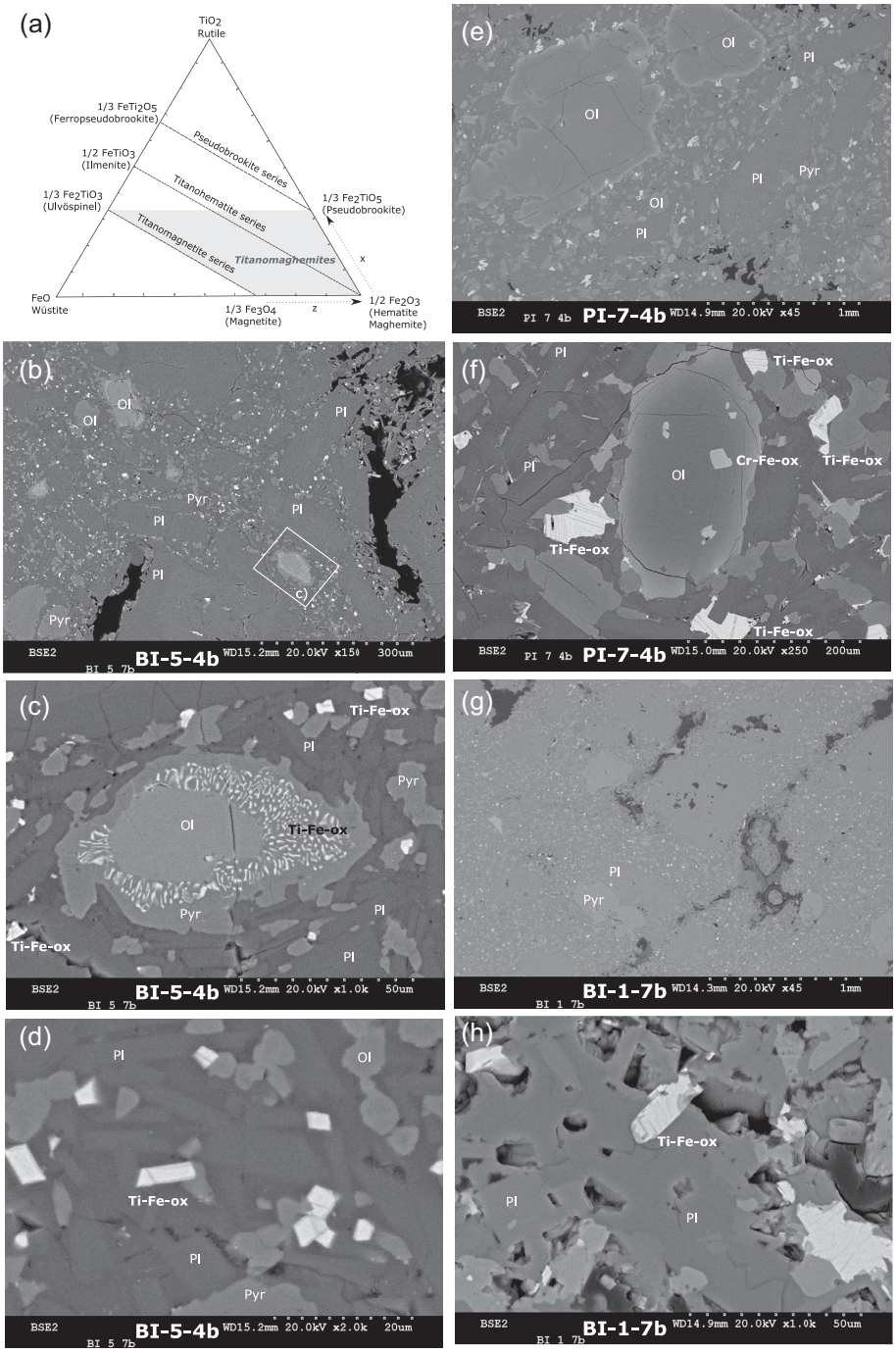

Figure 12. (a) Ternary diagram of the iron-titanium oxides, showing the composition of the different solid solution series in igneous rocks (modified from McElhinny & McFadden 2000). Grey area represents the (Ti)maghemite composition. Z is the oxidation level and X the Ti content. (b) General view of BI-5.4b, (c and d) details of the iron-oxides present, vermicular and euhedral with exsolution lamellae grains; lamellae enriched in Ti (ilmenite) are slightly darker than the Ti-poor iron oxide grain respectively. (e) General view of PI-7–4b and (f) detail of exsolved titanium iron oxides. (e) General view of BI-1–7b and (f) detail of exsolved titanium iron oxides. Back-scattered electron images of SEM with qualitative EDX analyses. Pl, plagioclase; Pyr, pyroxene; Ol, olivine; Ti-Fe-ox, titanium–iron oxide. Cr–Fe oxide, chromite. Scale is at the bottom right as aligned dots, their total length marks the μm in every picture.

5.2 Magnetic anisotropy; kinematic model of magma emplacement

Due to time limitations, sampling was concentrated in the centre of lava flows on Bridgeman Island and in a vertical section in the plateau lavas of Penguin Island. The orientation of the magnetic ellipsoid will be described based on the magnetic lineation orientation (mean of k_{max} axes) since it is well clustered on a horizontal plane, except in BI-5 and 6 (clustering of magnetic lineation occurs on the lava flow plane, although in BI-5, the lava flow plane is almost horizontal, Fig. 6). The average of the magnetic lineation on Bridgeman Island is clearly similar to the orientation of the spreading axis of the Bransfield Basin (orange line in the map of Fig. 13) in three

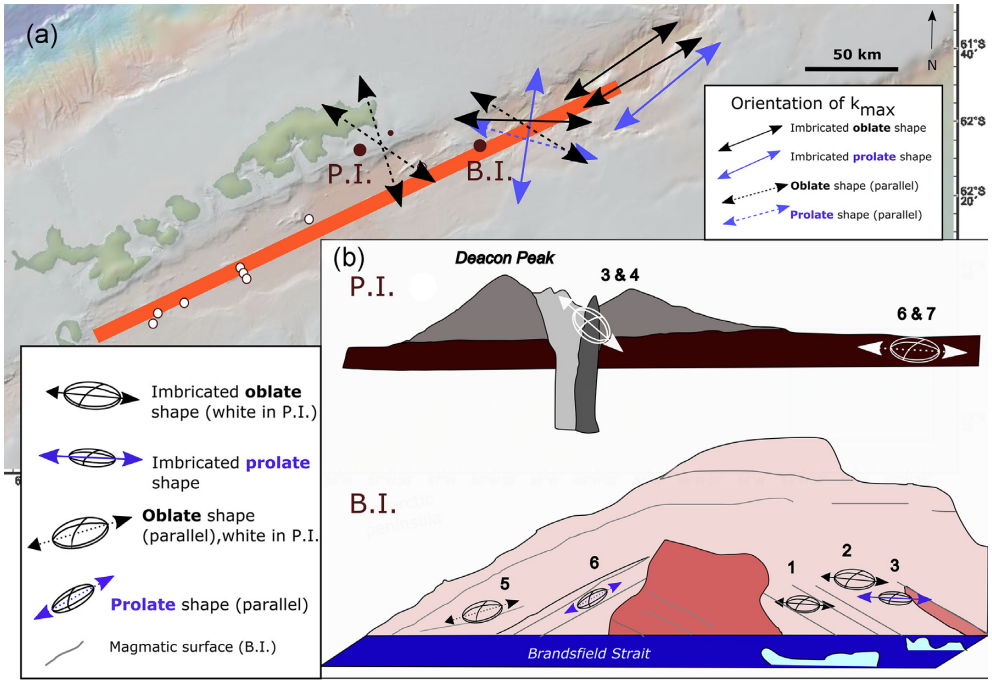

Figure 13. Schematic representation of the magnetic lineation in (a) map view of the lavas and (b) in cross-section (not to scale) on Penguin (P.I.) and Bridgeman (B.I.) islands of selected sites. On Penguin Island the volcanic plug ellipsoid is also added (centre of the island). Continuous (discontinuous) line with arrow: magnetic lineation in imbricated (parallel to lava surface) ellipsoids. Black: oblate shape, purple: prolate shape. Orange line in (a): simplification of the orientation of the spreading axis in the Bransfield Basin.

sites (sites 1–3), and it is close to the perpendicular direction in the older plateau lavas of Penguin Island and two sites in Bridgeman Island (sites 5 and 6).

The relationship between the magnetic lineation and the magmatic flow direction has been largely discussed previously, some authors found that k_{min} axes indicate the lava flow in palaeosurface with larger tilts (Boiron *et al.* 2013). However, results suggest that magnetic lineation can be a good indicator of lava flow when axes distribute in a horizontal plane (results in Caballero-Miranda *et al.* 2016).

We compare our results with studies performed in thicker lava flows and models of strain ellipses (Caballero-Miranda *et al.* 2016). In such studies, the origin of the flow is known. The 2-D models that better explain their observations relate to flow dynamics. The models show a lower positive and an upper opposed imbrication to the flow, separated by an intermediate zone of lowest degree of anisotropy. Positive imbrication occurs when the magnetic ellipse in 2-D is inclined towards the flow source, and opposed imbrication occurs when the magnetic ellipse in 2-D is inclined towards the end of the flow. The models represent three different cases, but in all of them the basal velocity is zero. In the first case, the maximum velocity is at the top of the flow, in other case the maximum velocity is somewhere in the middle of the flow, and the velocity at the top is zero (a crust on the lava has formed), and in the third case, the maximum velocity is somewhere in the middle of the flow and the velocity at the top is larger than zero. The upper boundary of the lower zone is considered where the maximum velocity of the flow is (V_{max}). The higher *Pj* values are in the lower zone. In addition, strain due to the weight of the lava is also considered in those models as pure shear (figs 11 and 12 in Caballero-Miranda *et al.* 2016).

Taking into account the magnetic foliation plane and the magnetic lineation orientation, the internal structure of these Quaternary lavas is either imbricated with respect to the lava plane, as in five sites of Bridgeman Island, or located with the same orientation of the lava flow, as in plateau lavas of Penguin Island and sites 5 and 6 on Bridgeman Island. The magnetic lineation on Bridgeman Island in the centre of the lava flows is either positively imbricated (horizontal in geographic coordinates) or close to the orientation of the tilted lava plane (Fig. 14a). The internal structure of the plateau lavas of Penguin Island is parallel to the flow plane, and slightly oppositely imbricated in samples with vesicles at the top of the two lava flows (Fig. 14b). The magnetic fabric in the lava plug of Penguin Island is also positively imbricated (Fig. 14c). The flow direction on Bridgeman Island is assumed to have been originated in the centre, and it is unknown in the plateau lavas of Penguin Island. Material of the plugs suggested to flow upwards in a dyke type fashion (Boiron *et al.* 2013).

The analysed sites show that: (i) samples at the centre of the lava flow have magnetic lineation parallel to the lava plane (represented with black grains parallel to lava planes on the right of the flow in Fig. 14a), which is related either to where the velocity is maximum and some vertical strain is exerted (as in fig. 11e in Caballero-Miranda *et al.* 2016, with velocities at the top and bottom of the model equaling zero), or in a flow with relative low velocity (as in fig. 12c in Caballero-Miranda *et al.* 2016), where velocity of the flow at the bottom is zero and at the top of the flow is larger than zero, (discontinuous grey line in Fig. 14a right and Fig. 14b). (ii) The sites with positive imbricated magnetic lineation with respect to the magma flow surface on Bridgeman Island, represented as black grains with a horizontal disposition in geographic coordinates on the left of the flow in Fig. 14(a), occur below the zone with maximum velocity in all cases represented in the strain models of Caballero-Miranda *et al.* (2016). The positive imbrication of the magnetic lineation with respect to the flow direction is also found in the volcanic plug of Penguin Island, suggesting that strain is occurring 'above' the maximum direction (as shown in all strain models in

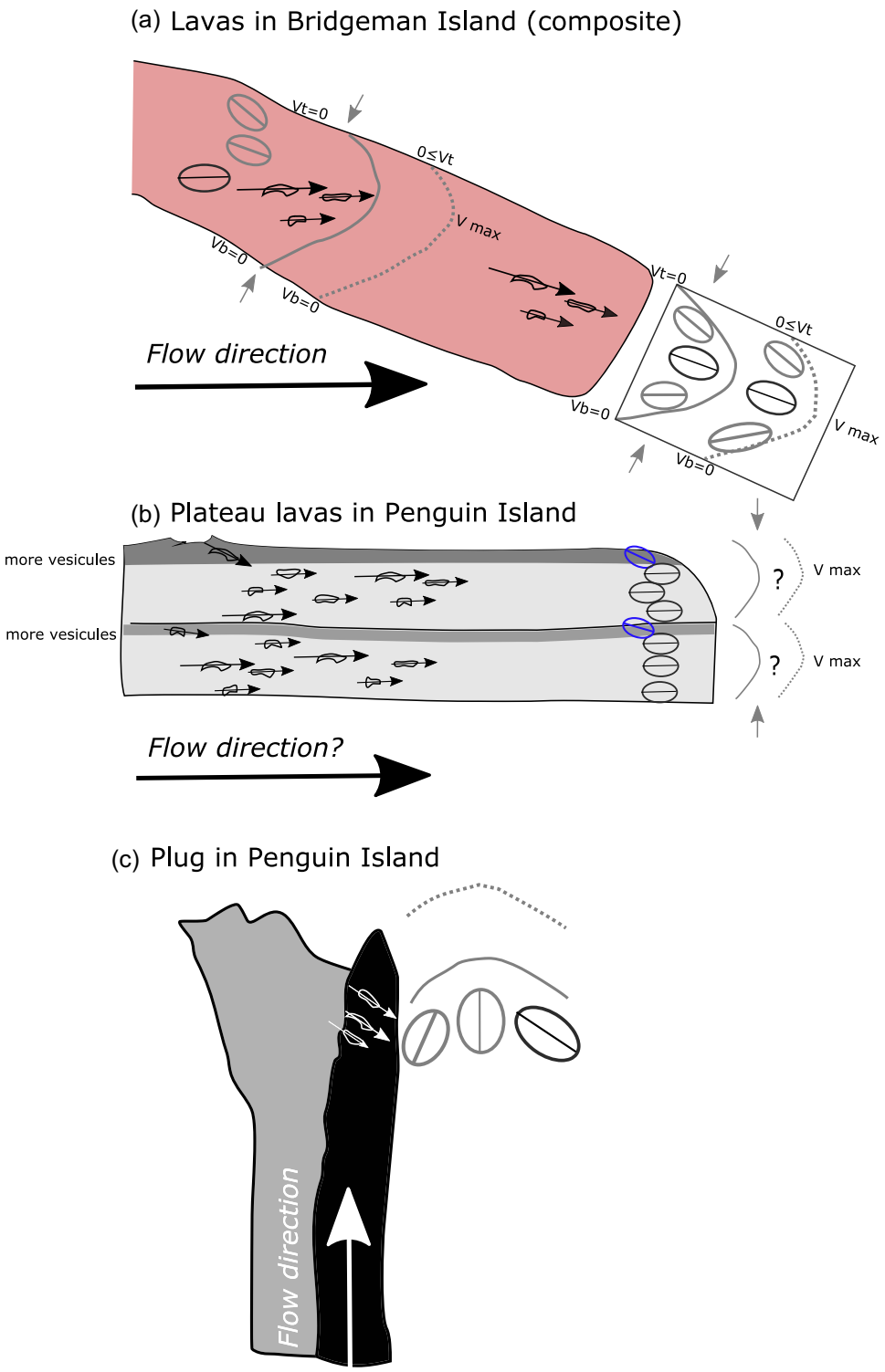

Figure 14. Representation of the orientation of magnetic lineation and strain according to models in Caballero-Miranda *et al.* (2016). Magnetite grains with black arrows represent the magnetic lineation. Ellipses represent the strain in those models, in black and purple, the ones that reflect the sampled sites. V_b: velocity at the bottom of the lava, V_t: velocity at the top. Continuous grey line represents those velocities in the lava: maximum in the centre, minimum at top and bottom ($V_b = V_t = 0$), the discontinuous grey line has $V_b = 0$ at the bottom but not at the top ($V_t > 0$). Small grey arrows indicate stress perpendicular to the lava surface (Caballero-Miranda *et al.* 2015). Idealization on (a) the lavas of Bridgeman Island, (b) the plateau lavas of Penguin Island and (c) the volcanic plug of Penguin Island.

Caballero-Miranda *et al.* (2016). (iii) Negative imbrication of the scoriaceous lavas at the top of the plateau flows on Penguin island.

Therefore, considering the strain in the models, we attempt to interpret the flow direction for the lavas as follows: On Bridgeman Island, the maximum velocity at the centre of the flow will impose a magnetic fabric parallel to the lava plane (BI-5 and 6). In other flows, the sampling is below the maximum flow velocity, where a positively imbricated magnetic lineation to the flow will be imposed (BI-1 to 3, 4 and 7). With respect to the Bransfield spreading axis, the flow directs in different directions: parallel, almost perpendicular and oblique (Figs 13 and 14).

The source for the plateau lavas on Penguin Island is not established, but the imbrication found in the more vesicular parts (top) is opposed to the flow (as described in Caballero-Miranda *et al.* 2016), this would indicate a SE–NW direction of the lava flow (Figs 7, 13 and 14). However, the lack of imbrication in the lower part of the flow is only present in the 2-D models that are perpendicular to the lava flow and are subjected to vertical strain. In these models, the top of the flow also shows a lack of imbrication. The lack of imbrication in the lower and central parts of the Penguin plateau lavas would be expected in non-viscous flows and/or where extremely vertical strain is exerted (not represented in the models of Caballero-Miranda *et al.* 2016). Finally, the magma flow that produces the plug in Penguin Island would be located below the maximum velocity flow in the sampling sites PI3 and 4, assuming a flow going upwards (Fig. 14c).

6 CONCLUSIONS

Studying the magnetic fabric and magnetic mineralogy helps to constrain the internal structure of magmatic rocks and flow directions.

Magnetic fabric in the volcanic edifices of Bridgeman and Penguin islands in the Bransfield backarc basin is mainly carried by Ti-poor magnetite, partially oxidized at low temperature to Ti-poor maghemite in low viscous magmas. The presence of hematite in some samples remains a possibility.

The internal structure of the magmatic flows based on the magnetic fabric and interpreted as imbricated strain with respect to the main flow suggests that the source on Bridgeman Island is at the centre, with varied flow directions respect to the Bransfield stretching axis.

The plateau lavas on Penguin Island reveal a constant orientation of the magnetic fabric, suggesting a strong vertical strain. The more vesicular parts show an imbrication with respect to the magma flow. If the imbrication follows models in previous studies, the flow would be mostly from the SE to the NW.

The volcanic domes are also imbricated with respect to an upwards flow, and the bombs show a scattered distribution, as expected in pyroclastic material.

ACKNOWLEDGEMENTS

This work is supported by the Projects CTM2014-57119-R and RTI2018-098099-B-I00 of the Spanish R&D National Plan. The authors acknowledge the facilities and logistic support of the Spanish Antarctic Program, particularly the Oceanographic Research Vessel Hesperides 2017 captain and crew. The AMS laboratory use and discussions at the University of Zaragoza (UZ) and at the University of Burgos were very useful. The *Servicio General de Apoyo a la Investigación-SAI* (UZ) is also acknowledged, together with E. Salvador from the SIdI of the Universidad Autónoma de Madrid. We are indebted to comments of reviewer A. Hirt, an anonymous reviewer and editor A. Biggin which contributed to improve the first version of the manuscript.

DATA AVAILABILITY

Data at sample level is available on request. Data at site level is on the paper.

The data underlying this article will be shared on reasonable request to the corresponding author.

REFERENCES

Aranguren, A., Cuevas, J., Tubia, J.M., Román-Berdiel, T., Casas-Sainz, A. & Casas-Ponsati, A., 2003. Granite laccolith emplacement in the Iberian arc: AMS and gravity study of the La Tojiza pluton (NW Spain), *J. Geol. Soc.,* **160**(3), 435–445.

Archanjo, C.J. & Launeau, P., 2004. Magma flow inferred from preferred orientations of plagioclase of the Rio Ceará-Mirim dyke swarm (NE Brazil) and its AMS significance, in *Magnetic Fabric: Methods and Applications,* Vol. **238,** pp. 285–298, eds Martín-Hernández, F., Jackson, M., Lüneburg, C. & Aubourg, C., Geological Society London Sp. Publ.

Baraldo, A, Rapalini, A.E., Böhnel, H. & Mena, M., 2003. Paleomagnetic study of Deception Island, South Shetland Islands, Antarctica, *Geophys. J. Int.,* **153,** 333–343.

Barker, P.F., 1982. The Cenozoic subduction history of the Pacific margin of the Antarctic Peninsula: ridge crest–trench interactions, *J. Geol. Soc.,* **139**(6), 787–801.

Barker, P.F., 2001. Scotia Sea regional tectonic evolution: implications for mantle flow and palaeocirculation, *Earth Sci. Rev.,* **55**(1–2), 1–39.

Bascou, J., Camps, P. & Dautria, J.M., 2005. Magnetic versus crystallographic fabrics in a basaltic lava flow, *J. Volc. Geotherm. Res.,* **145**(1–2), 119–135.

Biedermann, A.R., Pettke, T., Reusser, E. & Hirt, A.M., 2014. Anisotropy of magnetic susceptibility in natural olivine single crystals, *Geochem. Geophys. Geosyst.,* **15**(7), 3051–3065.

Biedermann, A.R., Pettke, T., Bender Koch, C. & Hirt, A.M., 2015. Magnetic anisotropy in clinopyroxene and orthopyroxene single crystals, *J. geophys. Res.,* **120**(3), 1431–1451.

Biedermann, A.R., Pettke, T., Angel, R.J. & Hirt, A.M., 2016. Anisotropy of magnetic susceptibility in alkali feldspar and plagioclase, *Geophys. Suppl. Mon. Not. R. astr. Soc.,* **205**(1), 479–489.

Birkenmajer, K., 1979. Age of the Penguin Island volcano, South Shetland Islands (West Antarctica), by the lichenometric method, *Bulletin De L Academie Polonaise Des Sciences-Serie Des Sciences De La Terre,* **27**(1–2), 69–76.

Birkenmajer, K., 1980. Age of the Penguin Island volcano, South Shetland Islands (West Antarctica), by the Lichenometric method, *Bulletin de la Academie Polonaise des Sciences - Serie des Sciences de la Terre,* **27,** 69–76.

Birkenmajer, K., 1994. Evolution of the Pacific margin of the northern Antarctic Peninsula: an overview, *Geol. Rundsch.,* **83,** 309–321.

Bohoyo, F. *et al.*, 2019. Morphological and geological features of Drake Passage, Antarctica, from a new digital bathymetric model, *J. Maps,* **15**(2), 49–59.

Boiron, T., Bascou, J., Camps, P., Ferré, E.C., Maurice, C., Guy, B., Gerbe, M.C. & Launeau, P., 2013. Internal structure of basalt flows: insights from magnetic and crystallographic fabrics of the La Palisse volcanics, French Massif Central, *Geophys. J. Int.,* **193**(2), 585–602.

Borradaile, G.J. & Jackson, M., 2004. Anisotropy of magnetic susceptibility (AMS): magnetic petrofabrics of deformed rocks, in *Magnetic Fabric: Methods and Applications,* Vol. **238**(1), pp. 299–360, eds Martín-Hernández, F., Jackson, M., Lüneburg, C. & Aubourg, C., Geological Society London Special Publications.

Bouchez, J.L., 1997. Granite is never isotropic: an introduction to AMS studies of granitic rocks, in *Granite: From Segregation of Melt to Emplacement*

Fabrics, pp. 95–112, eds Bouchez, J.-L., Hutton, D. & Stephens, W.E., Springer.

Caballero-Miranda, C.I., Alva-Valdivia, L.M., González-Rangel, J.A., Goguitchaishvili, A., Urrutia-Fucugauchi, J. & Kontny, A., 2016. Vertical AMS variation within basalt flow profiles from the Xitle volcano (Mexico) as indicator of heterogeneous strain in lava flows, *J. Volc. Geotherm. Res.,* **311,** 9–28.

Cañón-Tapia, E., Walker, G.P. & Herrero-Bervera, E., 1997. The internal structure of lava flows—insights from AMS measurements II: Hawaiian pahoehoe, toothpaste lava and'a'ā, *J. Volc. Geotherm. Res.,* **76**(1–2), 19–46.

Cañón-Tapia, E., 2004. Anisotropy of magnetic susceptibility of lava flows and dykes: a historical account, in *Magnetic Fabric: Methods and Applications,* Vol. **238**(1), pp. 205–225, eds Martín-Hernández, F., Jackson, M., Lüneburg, C. & Aubourg, C., Geological Society London Special Publications.

Catalán, M., Galindo-Zaldívar, J., Davila, J.M., Martos, Y.M., Maldonado, A., Gambôa, L. & Schreider, A.A., 2013. Initial stages of oceanic spreading in the Bransfield Rift from magnetic and gravity data analysis, *Tectonophysics,* **585,** 102–112.

Chadima, M. & Jelínek, V., 2008. Anisoft 4.2.—anisotropy data browser, *Contrib. Geophys. Geod.,* **38**(Special Issue), 38–41.

Dunlop, D.J. & Özdemir, Ö., 1997. *Rock Magnetism: Fundamentals and Frontiers*. Cambridge Univ. Press.

Dunlop, D.J., 2014. High-temperature susceptibility of magnetite: a new pseudo-single-domain effect, *Geophys. J. Int.,* **199**(2), 707–716.

Fanjat, G., Camps, P., Shcherbakov, V., Barou, F., Sougrati, M.T. & Perrin, M., 2012. Magnetic interactions at the origin of abnormal magnetic fabrics in lava flows: a case study from Kerguelen flood basalts, *Geophys. J. Int.,* **189**(2), 815–832.

Fisk, M.R., 1990, Volcanism in the Bransfield Strait, Antarctica, *J. South Am. Earth Sci.,* **3,** 91–101.

Fretzdorff, S., Worthington, T.J., Haase, K.M., Hékinian, R., Franz, L., Keller, R.A. & Stoffers, P., 2004. Magmatism in the Bransfield basin: rifting of the South Shetland Arc?, *J. geophys. Res.,* **109**(B12208), doi:10.1029/2004JB003046.

Galé, C. *et al.*, 2014. Quaternary volcanism in Deception Island (Antarctica): south Shetland Trench subduction-related signature in the Bransfield Basin back arc domain, *Boletín Geológico y Minero,* **125**(1), 31–52.

Galindo-Zaldívar, J., Gamboa, L., Maldonado, A., Nakao, S. & Bochu, Y., 2006, Bransfield Basin tectonic evolution, in *Antarctica,* pp. 243–248, eds Fütterer, D.K., Damaske, D., Kleinschmidt, G., Miller, H. & Tessensohn, F., Springer.

Gràcia, E., Canals, M., Farràn, M.L., Prieto, M.J., Sorribas, J. & Team, Gebra., 1996. Morphostructure and evolution of the central and eastern Bransfield basins (NW Antarctic Peninsula), *Mar. Geophys. Res.,* **18**(2–4), 429–448.

Goguitchaichvili, A., Morales, J., Urrutia-Fucugauchi, J. & Soler, A.M., 2001. On the use of continuous thermomagnetic curves in paleomagnetism: a cautionary note, *Comptes Rendus de l'Académie des Sciences-Series IIA-Earth and Planetary Science,* **333**(11), 699–704.

González-Casado, J.M., Giner-Robles, J.L. & López-Martínez, J., 2000. Bransfield Basin, Antarctic Peninsula: not a normal backarc basin, *Geology,* **28**(11), 1043–1046.

González-Ferrán, O., 1985. Volcanic and tectonic evolution of the northern Antarctic Peninsula—Late Cenozoic to Recent, *Tectonophysics,* **114**(1–4), 389–409.

González-Ferrán, O. & Katsui, Y., 1970. Estudio entegral del volcanismo Cenozoico Superior de las Islas Shetland del Sur, Antarctica, *Inst. antart. chil. Ser. cient.,* **1,** 123–174.

Henry, B., Plenier, G. & Camps, P., 2003. Post-emplacement tilting of lava flows inferred from magnetic fabric study: the example of Oligocene lavas in the Jeanne d'Arc Peninsula (Kerguelen islands), *J. Volc. Geotherm. Res.,* **127**(1–2), 153–164.

Hrouda, F., 2003. Indices for numerical characterization of the alteration processes of magnetic minerals taking place during investigation of temperature variation of magnetic susceptibility, *Stud. Geophys. Geod.,* **47**(4), 847–861.

Hrouda, F., Chlupáčová, M., Schulmann, K., Šmíd, J. & Závada, P., 2005. On the effect of lava viscosity on the magnetic fabric intensity in alkaline volcanic rocks, *Stud. Geophys. Geod.,* **49**(2), 191–212.

Ihmlé, P.F., Hirt, A.M., Lowrie, W. & Dietrich, D., 1989. Inverse magnetic fabric in deformed limestones of the Morcles Nappe, Switzerland, *Geophys. Res. Lett.,* **16**(12), 1383–1386.

Jelinek, V., 1981. Characterization of the magnetic fabric of rocks, *Tectonophysics,* **79**(3–4), T63–T67.

Keller, R.A., Fisk, M.R., Smellie, J.L., Strelin, J.A. & Lawver, L.A., 2002. Geochemistry of back arc basin volcanism in Bransfield Strait, Antarctica: subducted contributions and along-axis variations, *J. geophys. Res.,* **107**(B8), ECV–4.

Kraus, S., Kurbatov, A. & Yates, M., 2013. Geochemical signatures of tephras from Quaternary Antarctic Peninsula volcanoes, *Andean Geol.,* **40**(1), 1–40.

Lattard, D., Engelmann, R., Kontny, A. & Sauerzapf, U., 2006. Curie temperatures of synthetic titanomagnetites in the Fe-Ti-O system: effects of composition, crystal chemistry, and thermomagnetic methods, *J. geophys. Res.,* **111**(B12), doi:10.1029/2006JB004591.

Lüneburg, C.M., Lampert, S.A., Lebit, H.D., Hirt, A.M., Casey, M. & Lowrie, W., 1999. Magnetic anisotropy, rock fabrics and finite strain in deformed sediments of SW Sardinia (Italy), *Tectonophysics,* **307**(1–2), 51–74.

Maestro, A., Somoza, L., Rey, J., Martínez-Frías, J. & López-Martínez, J., 2007. Active tectonics, fault patterns, and stress field of Deception Island: a response to oblique convergence between the Pacific and Antarctic plates, *J. South Am. Earth Sci.,* **23**(2–3), 256–268.

Maldonado, A., Larter, R.D. & Aldaya, F., 1994. Forearc tectonic evolution of the South Sheltands margin, Antarctic Peninsula, *Tectonics,* **13**(6), 1345–1370.

McElhinny, M.W. & McFadden, P.L., 2000. *Paleomagnetism: Continents And Oceans,* International Geophysics series, Vol. 73. Academic Press.

Moskowitz, B.M., 1981. Methods for estimating Curie temperatures of titanomaghemites from experimentalJs-T data, *Earth planet. Sci. Lett.,* **53**(1), 84–88.

Nagaraju, E. & Parashuramulu, V., 2019. AMS studies on a 450 km long 2216 Ma dyke from Dharwar craton, India: implications to magma flow, *Geosci. Front.,* **10**(5), 1931–1939.

Özdemir, Ö., Dunlop, D.J. & Moskowitz, B.M., 1993. The effect of oxidation on the Verwey transition in magnetite, *Geophys. Res. Lett.,* **20**(16), 1671–1674.

Oliva-Urcia, B. *et al.*, 2015. Paleomagnetism from Deception Island (South Shetlands archipelago, Antarctica), new insights into the interpretation of the volcanic evolution using a geomagnetic model, *Int. J. Earth Sci.,* **105**(5), 1353–1370.

Pańczyk, M. & Nawrocki, J., 2011. Pliocene age of the oldest basaltic rocks of Penguin Island (South Shetland Islands, northern Antarctic Peninsula), *Geol. Quart.,* **55**(4), 335–344.

Petrovský, E. & Kapička, A., 2006. On determination of the Curie point from thermomagnetic curves, *J. geophys. Res.,* **111**(B12S27), doi:10.1029/2006JB004507.

Plenier, G., Camps, P., Henry, B. & Ildefonse, B., 2005. Determination of flow directions by combining AMS and thin-section analyses: implications for Oligocene volcanism in the Kerguelen Archipelago (southern Indian Ocean), *Geophys. J. Int.,* **160**(1), 63–78.

Pueyo-Anchuela, Ó. *et al.*, 2014. Application of AMS for reconstruction of the geological evolution of recent volcanic systems: case of Deception Island (South Shetland Islands, Antarctica), *Tectonophysics,* **626,** 69–85.

Raposo, M.I.B. & Berquó, T.S., 2008. Tectonic fabric revealed by AARM of the proterozoic mafic dike swarm in the Salvador city (Bahia State): são Francisco Craton, NE Brazil, *Phys. Earth planet. Inter.,* **167**(3–4), 179–194.

Raposo, M.I.B., 2020. Emplacement of dike swarms from the island of Ilhabela (SE Brazil) and its relationship with the South Atlantic Ocean opening revealed by magnetic fabrics, *Phys. Earth planet. Inter.,* **301,** 106471.

Rochette, P., 1987. Magnetic susceptibility of the rock matrix related to magnetic fabric studies, *J. Struct. Geol.,* **9**(8), 1015–1020.

Román-Berdiel, T., Aranguren, A., Cuevas, J. & Tubıa, J.M., 1998. Compressional granite-emplacement model: structural and magnetic study of the Trives Massif (NW Spain), *Lithos,* **44**(1–2), 37–52.

Román-Berdiel, T., Casas, A.M., Oliva-Urcia, B., Pueyo, E.L. & Rillo, C., 2004. The main Variscan deformation event in the Pyrenees: new data from the structural study of the Bielsa granite, *J. Struct. Geol.,* **26**(4), 659–677.

Sant' Ovaia, H., Bouchez, J.L., Noronha, F., Leblanc, D. & Vigneresse, J.L., 2001. Composite-laccolith emplacement of the post-tectonic Vila Pouca de Aguiar granite pluton (northern Portugal): a combined AMS and gravity study, in *The Fourth Hutton Symposium on the Origin of Granites and Related Rocks,* Special Papers-Geological Society of America, Vol. 350, pp. 123–138, eds Barbarin, B., Edryd Stephens, W., Bouchez, J.-L., Clarke, D.B., Cuney, M. & Martin, H., Geological Society of America.

Schmidt, V., Hirt, A.M., Rosselli, P. & Martín-Hernández, F., 2007. Separation of diamagnetic and paramagnetic anisotropy by high-field, low-temperature torque measurements, *Geophys. J. Int.,* **168**(1), 40–47.

Smellie, J.L., Panter, K.S. & Geyer, A.eds., 2021. Volcanism in Antarctica: 200 million years of subduction, rifting and continental break-up, *Geological Society, London, Memoirs,* **55,**.

Soriano, C., Beamud, E., Garcés, M. & Ort, M.H., 2016. 'Anomalous' magnetic fabrics of dikes in the stable single domain/superparamagnetic threshold, *Geophys. J. Int.,* **204**(2), 1040–1059.

Stevenson, C.T., O'Driscoll, B., Holohan, E.P., Couchman, R., Reavy, R.J. & Andrews, G.D., 2008. The structure, fabrics and AMS of the Slieve Gullion ring-complex, Northern Ireland: testing the ring-dyke emplacement model, *Geol. Soc., Lond., Spec. Publ.,* **302**(1), 159–184.

Tarling, D. & Hrouda, F.eds., 1993. *Magnetic Anisotropy of Rocks*. Springer Science & Business Media.

Tauxe, L., Mullender, T.A.T. & Pick, T., 1996. Potbellies, wasp-waists, and superparamagnetism in magnetic hysteresis, *J. geophys. Res.,* **101**(B1), 571–583.

Weil, A.B. & Van der Voo, R., 2002. Insights into the mechanism for orogen-related carbonate remagnetization from growth of authigenic Fe-oxide: a scanning electron microscopy and rock magnetic study of Devonian carbonates from northern Spain, *J. geophys. Res.,* **107**(B4), 2063, doi:10.1029/2001JB000200.